Nanofiber-mediated chiral radiative coupling between two atoms

Fam Le Kien

Quantum Systems Unit, Okinawa Institute of Science and Technology Graduate University, Onna, Okinawa 904-0495, Japan

A. Rauschenbeutel

Vienna Center for Quantum Science and Technology, Institute of Atomic and Subatomic Physics,
Vienna University of Technology, Stadionallee 2, 1020 Vienna, Austria

We investigate the radiative coupling between two two-level atoms with arbitrarily polarized dipoles in the vicinity of a nanofiber. We present a systematic derivation for the master equation, the single- and cross-atom decay coefficients, and the dipole-dipole interaction coefficients for the atoms interacting with the vacuum of the field in the guided and radiation modes of the nanofiber. We study numerically the case where the atomic dipoles are circularly polarized. In this case, the rate of emission depends on the propagation direction along the fiber axis and, hence, the radiative interaction between the atoms is chiral. We examine the time evolution of the atoms for different initial states. We calculate the fluxes and mean numbers of photons spontaneously emitted into guided modes in the positive and negative directions of the fiber axis. We show that the chiral radiative coupling modifies the collective emission of the atoms. We observe that the modifications strongly depend on the initial state of the atomic system, the radiative transfer direction, the distance between the atoms, and the distance from the atoms to the fiber surface.

I. INTRODUCTION

Radiative coupling between two atoms (or molecules) has been a topic of great interest for the past several decades. The range and strength of the coupling can be enhanced by means of dressing the environment. A typical nonradiative Förster energy transfer range of $\leqslant 10$ nm was surpassed by use of localized plasmons, whispering gallery modes, or microcavities [1–12]. Very fast (on the picosecond time scale) energy transfer was recorded in systems with quantum dots [13] and strongly bound excitons [14]. Plasmon-assisted communication was demonstrated between donor-acceptor pairs across 120-nm-thick metal films [15] and between fluorophores on top of a silver film over distances up to 7 μm [16]. The recent directions of research on dipole-dipole interaction now encompass areas of few-atom spectroscopy [17,18], near-field optics [19], and subwavelength-resolution nano-optics [20]. The effects of a nanosphere on the dipole-dipole interaction have been studied [21,22]. A form of telegraphy on a dielectric microplanet has been proposed [3]. It is clear that the range of such telegraphy can be increased arbitrarily if one uses nanofibers.

The effects of a nanofiber on spontaneous emission of a two-level atom [23,24], a multilevel atom [25], and two two-level atoms [26] have been studied. It has been shown that spontaneous emission and scattering from an atom with a circular dipole in the vicinity of a nanofiber can be asymmetric with respect to the opposite axial propagation directions [27–32]. These directional effects are the signatures of spin-orbit coupling of light [33–37] carrying transverse spin angular momentum [37,38]. They are due to the existence of a nonzero longitudinal component of the nanofiber guided field, which oscillates in phase quadrature with respect to the radial transverse component. The possibility of directional emission from an atom into propagating radiation modes of a nanofiber and the possibility of generation of a lateral force on the atom have been pointed out [31]. The direction-dependent emission and absorption of photons lead to chiral quantum optics [39].

It has been shown that substantial coupling between two atoms can survive over long interatomic distances due to guided modes [26]. The chiral coupling between atoms has been studied in the framework of one-dimensional waveguide bath models [40–46], where radiation modes were completely [40–44] or partially [45,46] neglected. In closely related studies, the chiral effect in spontaneous emission of a single atom [47] and the radiative transfer between two atoms [48] in front of a dielectric surface have also been investigated.

In this paper, we study radiative coupling between two two-level atoms with arbitrarily polarized dipoles in the vicinity of a nanofiber. Unlike Ref. [26], our treatment incorporates rotating induced dipoles. In addition, our treatment is more general than the previous studies [40–42,44,45] in the sense that we use a three-dimensional fiber model and take into account the effects of radiation modes on the decay rate coefficients and the dipole-dipole interaction coefficients. We focus on the case where the atomic dipoles are circularly polarized and, consequently, the rate of emission depends on the propagation direction and the radiative interaction between the atoms is chiral. In order to get insight into this chiral coupling, we look at the decay behavior of the atoms as well as the fluxes and numbers of photons emitted into guided modes.

The paper is organized as follows. In Sec. II we describe the model of two two-level atoms with arbitrarily polarized dipoles in the vicinity of a nanofiber. In Sec. III we derive the basic equations for the interaction between the atoms and the field in guided and radiation modes. In Sec. IV we present the results of numerical calculations. Our conclusions are given in Sec. V.

II. MODEL

A. Quantization of the field around a nanofiber

We consider a fiber that has a cylindrical silica core of radius a and refractive index $n_1 > 1$ and an infinite vacuum
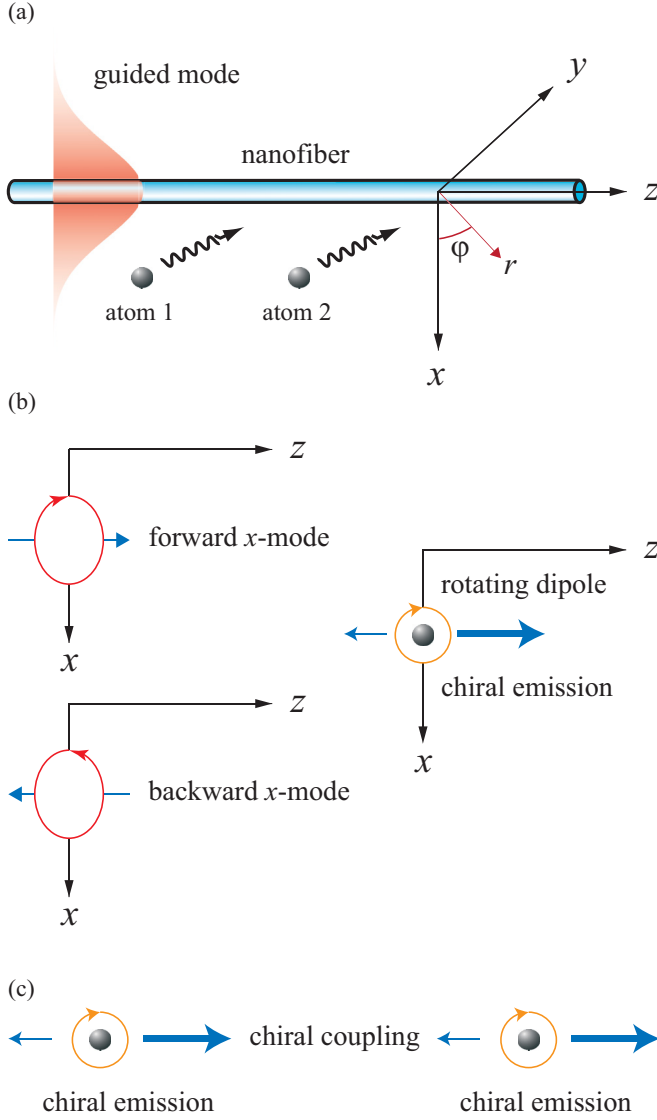
(a)

(b)

(c)

FIG. 1. (a) Two two-level atoms in the vicinity of a nanofiber. (b) Chiral emission of an individual atom with a dipole rotating in the meridional plane. (c) Chiral coupling between two atoms with dipoles rotating in the meridional plane.

cladding of refractive index $n_2 = 1$ [see Fig. 1(a)]. We use the Cartesian coordinates $\{x,y,z\}$ and the cylindrical coordinates $\{r,\varphi,z\}$ with z being the fiber axis. In view of the very low losses of silica in the wavelength range of interest, we neglect material absorption.

The continuum field quantization follows the procedures presented in Ref. [49]. In the presence of the nanofiber, the positive-frequency part $\mathbf{E}^{(+)}$ of the electric component of the field can be decomposed into the contributions $\mathbf{E}_{\text{gd}}^{(+)}$ and $\mathbf{E}_{\text{rad}}^{(+)}$ from guided and radiation modes, respectively, as

$$\mathbf{E}^{(+)} = \mathbf{E}_{\text{gd}}^{(+)} + \mathbf{E}_{\text{rad}}^{(+)}. \tag{1}$$

Regarding guided modes, we assume that the single-mode condition [50] is satisfied for a finite bandwidth of the field frequency ω around a characteristic atomic transition frequency ω_0. In this case, the nanofiber supports only

the hybrid fundamental modes HE$_{11}$ corresponding to the wavelength $\lambda = 2\pi c/\omega$ [50]. We label each guided mode by an index $\mu = (\omega f l)$, where $f = +,-$ denotes the forward or backward propagation direction, and $l = +,-$ denotes the counterclockwise or clockwise polarization. When we quantize the field in the guided modes, we obtain the following expression for $\mathbf{E}_{\text{gd}}^{(+)}$ in the interaction picture:

$$\mathbf{E}_{\text{gd}}^{(+)} = i \int_0^\infty d\omega \sum_{fl} \sqrt{\frac{\hbar\omega\beta'}{4\pi\epsilon_0}}\, a_\mu \mathbf{e}^{(\mu)} e^{-i(\omega t - f\beta z - l\varphi)}. \tag{2}$$

Here, β is the longitudinal propagation constant, β' is the derivative of β with respect to ω, a_μ is the respective photon annihilation operator, and $\mathbf{e}^{(\mu)} = \mathbf{e}^{(\mu)}(r,\varphi)$ is the electric-field profile function of the guided mode μ in the classical problem. The constant β is determined by the fiber eigenvalue equation (A1). The operators a_μ and $a_\mu^\dagger$ satisfy the continuous-mode bosonic commutation rules $[a_\mu, a_{\mu'}^\dagger] = \delta(\omega - \omega')\delta_{ff'}\delta_{ll'}$. The normalization of $\mathbf{e}^{(\mu)}$ is given by

$$\int_0^{2\pi} d\varphi \int_0^\infty n_{\text{ref}}^2 |\mathbf{e}^{(\mu)}|^2 r\, dr = 1. \tag{3}$$

Here, $n_{\text{ref}}(r) = n_1$ for $r < a$, and $n_{\text{ref}}(r) = n_2$ for $r > a$. The explicit expression for the guided mode function $\mathbf{e}^{(\mu)}$ is given in Appendix A.

Unlike the case of guided modes, in the case of radiation modes, the longitudinal propagation constant β for each value of ω can vary continuously, from $-k$ to k, where $k = \omega/c$ is the wavelength of light in free space. We label each radiation mode by an index $\nu = (\omega\beta ml)$, where $m = 0, \pm 1, \pm 2, \ldots$ is the mode order and $l = \pm$ is the mode polarization. When we quantize the field in the radiation modes, we obtain the following expression for $\mathbf{E}_{\text{rad}}^{(+)}$ in the interaction picture:

$$\mathbf{E}_{\text{rad}}^{(+)} = i \int_0^\infty d\omega \int_{-k}^k d\beta \sum_{ml} \sqrt{\frac{\hbar\omega}{4\pi\epsilon_0}}\, a_\nu \mathbf{e}^{(\nu)} e^{-i(\omega t - \beta z - m\varphi)}. \tag{4}$$

Here, a_ν is the respective photon annihilation operator, and $\mathbf{e}^{(\nu)} = \mathbf{e}^{(\nu)}(r,\varphi)$ is the electric-field profile function of the radiation mode ν in the classical problem. The operators a_ν and $a_\nu^\dagger$ satisfy the continuous-mode bosonic commutation rules $[a_\nu, a_{\nu'}^\dagger] = \delta(\omega - \omega')\delta(\beta - \beta')\delta_{mm'}\delta_{ll'}$. The normalization of $\mathbf{e}^{(\nu)}$ is given by

$$\int_0^{2\pi} d\varphi \int_0^\infty n_{\text{ref}}^2 [\mathbf{e}^{(\nu)}\mathbf{e}^{(\nu')*}]_{\beta=\beta',m=m',l=l'} r\, dr = \delta(\omega - \omega'). \tag{5}$$

The explicit expression for the radiation mode function $\mathbf{e}^{(\nu)}$ is given in Appendix B.

B. Two atoms interacting with the field

Consider two two-level atoms with the identical transition frequency ω_0. We label the atoms by the index $j = 1,2$. The atoms are located at points $\mathbf{R_1} \equiv \{r_1,\varphi_1,z_1\}$ and $\mathbf{R_2} \equiv \{r_2,\varphi_2,z_2\}$ [see Fig. 1(a)]. In the interaction picture, the electric dipole of atom j is given by $\mathbf{D}_j = \mathbf{d}_j^* \sigma_j e^{-i\omega_0 t} + \mathbf{d}_j \sigma_j^\dagger e^{i\omega_0 t}$.

Here, the operators $\sigma_j = |-\rangle_{jj}\langle+|$ and $\sigma_j^\dagger = |+\rangle_{jj}\langle-|$ describe respectively the downward and upward transitions of atom j, and $\mathbf{d}_j$ is the corresponding dipole matrix element. The notations $|+\rangle_j$ and $|-\rangle_j$ stand for the upper and lower states, respectively, of atom j. In general, the dipole matrix element $\mathbf{d}_j$ can be a complex vector. The basis states of the two-atom system can be written as $|s_1 s_2\rangle = |s_1\rangle_1 \otimes |s_2\rangle_2$, where $s_1, s_2 = \pm$.

For brevity, we use the index $\alpha = \mu, \nu$ as a common label for the guided modes μ and the radiation modes ν. In addition, we use the notation $\sum_\alpha = \sum_\mu + \sum_\nu$, where $\sum_\mu = \int_0^\infty d\omega \sum_{fl}$ and $\sum_\nu = \int_0^\infty d\omega \int_{-k}^k d\beta \sum_{ml}$ are generalized summations over guided and radiation modes, respectively. In the interaction picture, the Hamiltonian for the atom-field interaction in the dipole approximation can be written as

$$H_{\text{int}} = -i\hbar \sum_{\alpha j}(G_{\alpha j}\sigma_j^\dagger a_\alpha e^{-i(\omega-\omega_0)t} - \text{H.c.})$$
$$- i\hbar \sum_{\alpha j}(\tilde{G}_{\alpha j}\sigma_j a_\alpha e^{-i(\omega+\omega_0)t} - \text{H.c.}). \quad (6)$$

Here, the coefficient $G_{\alpha j}$ characterizes the coupling of atom j with mode α via the corotating terms $\sigma_j^\dagger a_\alpha$ and $\sigma_j a_\alpha^\dagger$. The expressions for $G_{\alpha j}$ with $\alpha = \mu, \nu$ are

$$G_{\mu j} = \sqrt{\frac{\omega\beta'}{4\pi\hbar\epsilon_0}}\,[\mathbf{d}_j \cdot \mathbf{e}^{(\mu)}(r_j, \varphi_j)]e^{i(f\beta z_j + l\varphi_j)},$$
$$G_{\nu j} = \sqrt{\frac{\omega}{4\pi\hbar\epsilon_0}}\,[\mathbf{d}_j \cdot \mathbf{e}^{(\nu)}(r_j, \varphi_j)]e^{i(\beta z_j + m\varphi_j)}. \quad (7)$$

The coefficient $\tilde{G}_{\alpha j}$ describes the coupling of atom j with mode α via the counterrotating terms $\sigma_j a_\alpha$ and $\sigma_j^\dagger a_\alpha^\dagger$. The expressions for $\tilde{G}_{\alpha j}$ with $\alpha = \mu, \nu$ are obtained from Eqs. (7) by replacing the dipole matrix element $\mathbf{d}_j$ with its complex conjugate $\mathbf{d}_j^*$, that is,

$$\tilde{G}_{\mu j} = \sqrt{\frac{\omega\beta'}{4\pi\hbar\epsilon_0}}\,[\mathbf{d}_j^* \cdot \mathbf{e}^{(\mu)}(r_j, \varphi_j)]e^{i(f\beta z_j + l\varphi_j)},$$
$$\tilde{G}_{\nu j} = \sqrt{\frac{\omega}{4\pi\hbar\epsilon_0}}\,[\mathbf{d}_j^* \cdot \mathbf{e}^{(\nu)}(r_j, \varphi_j)]e^{i(\beta z_j + m\varphi_j)}. \quad (8)$$

III. BASIC EQUATION

A. Master equation for the atoms

We call $\mathcal{O}$ an arbitrary atomic operator. The Heisenberg equation for this operator is

$$\dot{\mathcal{O}} = \sum_{\alpha j}(G_{\alpha j}[\sigma_j^\dagger, \mathcal{O}]a_\alpha e^{-i(\omega-\omega_0)t}$$
$$+ \tilde{G}_{\alpha j}[\sigma_j, \mathcal{O}]a_\alpha e^{-i(\omega+\omega_0)t}$$
$$+ G_{\alpha j}^* a_\alpha^\dagger[\mathcal{O}, \sigma_j]e^{i(\omega-\omega_0)t}$$
$$+ \tilde{G}_{\alpha j}^* a_\alpha^\dagger[\mathcal{O}, \sigma_j^\dagger]e^{i(\omega+\omega_0)t}). \quad (9)$$

The Heisenberg equation for the photon annihilation operator a_α is

$$\dot{a}_\alpha = \sum_j G_{\alpha j}^* \sigma_j e^{i(\omega-\omega_0)t} + \sum_j \tilde{G}_{\alpha j}^* \sigma_j^\dagger e^{i(\omega+\omega_0)t}. \quad (10)$$

We integrate Eq. (10). Then, we obtain

$$a_\alpha(t) = a_\alpha(t_0) + \sum_j G_{\alpha j}^* \int_{t_0}^t dt'\, \sigma_j(t')e^{i(\omega-\omega_0)t'}$$
$$+ \sum_j \tilde{G}_{\alpha j}^* \int_{t_0}^t dt'\, \sigma_j^\dagger(t')e^{i(\omega+\omega_0)t'}, \quad (11)$$

where t_0 is the initial time.

We consider the situation where the field is initially in the vacuum state. We assume that the evolution time $t - t_0$ and the characteristic atomic lifetime τ_a are large as compared to the optical period $2\pi/\omega_0$ and the light propagation time $|\mathbf{R}_2 - \mathbf{R}_1|/c$ between the two atoms. When the continuum of the guided and radiation modes is regular and broadband around the atomic frequency, the effect of the retardation is concealed [51], and the Markov approximation $\sigma_j(t') = \sigma_j(t)$ can be applied to describe the back action of the second and third terms in Eq. (11) on the atom. Under the condition $t - t_0 \gg 2\pi/\omega_0$, we calculate the integrals with respect to t' in the limit $t - t_0 \to \infty$. Then, Eq. (11) yields

$$a_\alpha(t) = a_\alpha(t_0)$$
$$+ \sum_j G_{\alpha j}^* \sigma_j(t)e^{i(\omega-\omega_0)t}\left[\pi\delta(\omega-\omega_0) - i\text{P}\frac{1}{\omega-\omega_0}\right]$$
$$+ \sum_j \tilde{G}_{\alpha j}^* \sigma_j^\dagger(t)e^{i(\omega+\omega_0)t}\left[\pi\delta(\omega+\omega_0) - i\text{P}\frac{1}{\omega+\omega_0}\right], \quad (12)$$

where the notation P stands for the principal value. We insert Eq. (12) into Eq. (9) and neglect fast-oscillating terms. Then, we obtain the Heisenberg-Langevin equation

$$\dot{\mathcal{O}} = \frac{1}{2}\sum_{ij}\gamma_{ij}([\sigma_i^\dagger, \mathcal{O}]\sigma_j + \sigma_i^\dagger[\mathcal{O}, \sigma_j])$$
$$+ i\sum_{ij}\Omega_{ij}[\sigma_i^\dagger\sigma_j, \mathcal{O}] + \xi_{\mathcal{O}}. \quad (13)$$

Here, the coefficients

$$\gamma_{ij} = 2\pi\sum_\alpha G_{\alpha i}G_{\alpha j}^*\delta(\omega-\omega_0) \quad (14)$$

and

$$\Omega_{ij} = -\text{P}\sum_\alpha\left[\frac{G_{\alpha i}G_{\alpha j}^*}{\omega-\omega_0} + (-1)^{\delta_{ij}}\frac{\tilde{G}_{\alpha i}^*\tilde{G}_{\alpha j}}{\omega+\omega_0}\right] \quad (15)$$

describe the decay rates and frequency shifts, respectively, and $\xi_{\mathcal{O}}$ is the noise operator.

Let ρ be the reduced density operator for the atomic system. When we use the Heisenberg-Langevin equation (13) and the relation $\text{Tr}[\mathcal{O}(t)\rho(0)] = \text{Tr}[\mathcal{O}(0)\rho(t)]$, we find the master

equation

$$\dot{\rho} = \frac{1}{2} \sum_{ij} \gamma_{ij} (2\sigma_j \rho \sigma_i^\dagger - \sigma_i^\dagger \sigma_j \rho - \rho \sigma_i^\dagger \sigma_j)$$
$$- i \sum_{ij} \Omega_{ij} [\sigma_i^\dagger \sigma_j, \rho]. \tag{16}$$

In deriving the above equation, we multiplied Eq. (13) with $\rho(0)$, took the trace of the result, replaced the form $\text{Tr}[\mathcal{O}_1(t)\mathcal{O}(t)\mathcal{O}_2(t)\rho(0)]$ by the form $\text{Tr}[\mathcal{O}_1(0)\mathcal{O}(0)\mathcal{O}_2(0)\rho(t)]$, transformed to move the operator $\mathcal{O}(0)$ to the first position in each operator product, and eliminated $\mathcal{O}(0)$.

Note that $\gamma_{ij} = \gamma_{ji}^*$ and $\Omega_{ij} = \Omega_{ji}^*$. The single-atom coefficients γ_{jj} and Ω_{jj} are real parameters. However, the cross-atom decay coefficient γ_{12} and the dipole-dipole interaction coefficient Ω_{12} are generally complex parameters in the case of arbitrarily polarized dipoles.

For two identical atoms with linearly polarized dipoles in free space, the cross-atom decay coefficient γ_{12} and the dipole-dipole interaction coefficient Ω_{12} are real. In this case, the populations of the superradiant and subradiant superposition states decay with the rates $\gamma_0 + |\gamma_{12}|$ and $\gamma_0 - |\gamma_{12}|$, respectively [52]. Here, γ_0 is the rate of single-atom decay in free space. Meanwhile, the energy splitting between the superradiant and subradiant states is determined by the dipole-dipole coupling coefficient Ω_{12} [52].

The above interpretation remains valid when the cross-atom decay coefficient γ_{12} and the dipole-dipole interaction coefficient Ω_{12} are complex parameters but have the same phase. Indeed, we can perform an appropriate transformation for the atomic operators to remove the phases of γ_{12} and Ω_{12} if these phases are equal to each other.

When the cross-atom decay coefficient γ_{12} and the dipole-dipole interaction coefficient Ω_{12} are complex parameters and have different phases, it is not easy to interpret the physical meaning of these coefficients individually. Indeed, the imaginary part of the complex cross-atom decay coefficient γ_{12} may affect the energy splitting between the superradiant and subradiant states, while the imaginary part of the complex dipole-dipole interaction coefficient Ω_{12} may affect the collective decay of atomic population.

The roles of the absolute value and phase of the cross-atom decay coefficient γ_{12} can be seen when we neglect the dipole-dipole interaction coefficient Ω_{12}. In this case, the phase of γ_{12} determines the relative phases between the component states $|+-\rangle$ and $|-+\rangle$ in the superradiant (symmetric) and subradiant (antisymmetric) superposition states, which decay separately from each other in the collective atomic dissipation process. Meanwhile, the absolute value of γ_{12} determines the modifications of the decay rates of the superradiant and subradiant states, caused by the collective effect.

The roles of the absolute value and phase of the dipole-dipole interaction coefficient Ω_{12} can be seen when we neglect the cross-atom decay coefficient γ_{12}. In this case, the phase of Ω_{12} determines the relative phases between the component states $|+-\rangle$ and $|-+\rangle$ in the one-excitation dressed states, which are defined as the eigenstates of the dipole-dipole

interaction operator. Meanwhile, the absolute value of Ω_{12} determines the energy splitting between these dressed states.

In order to get deeper insight into the roles of the absolute values and phases of the complex collective coupling coefficients γ_{12} and Ω_{12}, we perform the following analysis.

Let $\gamma_{12} = |\gamma_{12}| \exp(i\phi_\gamma)$ and $\Omega_{12} = |\Omega_{12}| \exp(i\phi_\Omega)$, where ϕ_γ and ϕ_Ω are the phases of the complex coefficients γ_{12} and Ω_{12}, respectively. We introduce the transformations $\tilde{\sigma}_1 = \sigma_1 \exp(i\phi_0)$ and $\tilde{\sigma}_2 = \sigma_2 \exp[i(\phi_\gamma + \phi_0)]$, where ϕ_0 is an arbitrary parameter. Then, we can rewrite Eq. (16) as

$$\dot{\rho} = \frac{1}{2} \sum_{ij} \tilde{\gamma}_{ij} (2\tilde{\sigma}_j \rho \tilde{\sigma}_i^\dagger - \tilde{\sigma}_i^\dagger \tilde{\sigma}_j \rho - \rho \tilde{\sigma}_i^\dagger \tilde{\sigma}_j)$$
$$- i \sum_{ij} \tilde{\Omega}_{ij} [\tilde{\sigma}_i^\dagger \tilde{\sigma}_j, \rho], \tag{17}$$

where $\tilde{\gamma}_{jj} = \gamma_{jj}$, $\tilde{\Omega}_{jj} = \Omega_{jj}$, $\tilde{\gamma}_{12} = |\gamma_{12}|$, and $\tilde{\Omega}_{12} = |\Omega_{12}| \exp[i(\phi_\Omega - \phi_\gamma)]$. It is clear that $\tilde{\gamma}_{jj}$, $\tilde{\Omega}_{jj}$, and $\tilde{\gamma}_{12}$ are real. However, when $|\Omega_{12}| \neq 0$ and $\phi_\Omega - \phi_\gamma \neq 0, \pm \pi$, the imaginary part of $\tilde{\Omega}_{12}$ is nonzero. It can be shown that the expression on the right-hand side of Eq. (17) contains the different direction-dependent excitation transfer terms $\tilde{\sigma}_1^\dagger \tilde{\sigma}_2 \rho$ and $\tilde{\sigma}_2^\dagger \tilde{\sigma}_1 \rho$ with the different coefficients $\tilde{\gamma}_{12} - 2\text{Im}(\tilde{\Omega}_{12})$ and $\tilde{\gamma}_{12} + 2\text{Im}(\tilde{\Omega}_{12})$, respectively. When $\tilde{\gamma}_{12} \neq 0$ and $\text{Im}(\tilde{\Omega}_{12}) \neq 0$, the left-right symmetry is broken. Thus, when $|\gamma_{12}| \neq 0$, $|\Omega_{12}| \neq 0$, and $\phi_\Omega - \phi_\gamma \neq 0, \pm \pi$, the interaction between the atoms through the field depends on the direction of energy transfer, i.e., it is chiral [40–45]. We note that, in the particular case where $\phi_\Omega - \phi_\gamma = \pi/2$ and $|\Omega_{12}| = |\gamma_{12}|/2$, we have $\text{Im}(\tilde{\Omega}_{12}) = \tilde{\gamma}_{12}/2$. In this case, the expression on the right-hand side of Eq. (17) contains the forward (left-to-right) excitation transfer term $\tilde{\sigma}_2^\dagger \tilde{\sigma}_1 \rho$ but not the backward (right-to-left) excitation transfer term $\tilde{\sigma}_1^\dagger \tilde{\sigma}_2 \rho$ [40–45].

The chirality in spontaneous emission and scattering from an atom with a circular dipole in the vicinity of a nanofiber has been studied in detail [27–32]. The origin of the chirality in these effects is that the nanofiber guided field has a nonzero longitudinal component, which oscillates in phase quadrature with respect to the radial transverse component. Due to this fact, at an arbitrary position on the x axis, the local polarization of the x-polarized modes is elliptical in the meridional plane zx [see the left part of Fig. 1(b)]. This leads to a nonzero local density of transverse spin angular momentum of light. Due to spin-orbit coupling of light [33–38], the sign of the local transverse spin density and, consequently, the sign of the local polarization ellipticity in the meridional plane zx are opposite for opposite propagation directions along the z axis [see the left part of Fig. 1(b)]. Note that the signs of these local characteristics for the x-polarized modes are also opposite for opposite sides of the x axis. Meanwhile, the local polarization of the y-polarized modes at an arbitrary position on the x axis is exactly linear and is aligned along the y axis. When an atom is located on the x axis and has a dipole rotating in the meridional plane zx, the symmetry of the combined nanofiber-atom system with respect to the opposite propagation directions along the fiber axis z is broken [see the right part of Fig. 1(b)]. Since the dipole vector of the atom is orthogonal to the local polarization vector of the y-polarized modes, the atom couples exclusively to the x-polarized modes.

Due to the breaking of the symmetry, the coupling is not symmetric with respect to the opposite propagation directions along the fiber axis. The atom emits predominantly a photon into the forward- or backward-propagating x-polarized mode that has a larger overlap between the electric field vector and the atomic electric dipole vector [see the right part of Fig. 1(b)]. In general, the asymmetry of the spontaneous emission rate with respect to opposite propagation directions, that is, the chirality in spontaneous emission, occurs when the ellipticity vector of the atomic dipole polarization overlaps with the local ellipticity vector of the field mode polarization at the position of the atom [27,47]. This condition implies that both the local polarization vector of the field and the dipole matrix element vector of the atom are complex vectors.

In the case of two atoms with arbitrarily polarized dipoles in the vicinity of a nanofiber, the chirality appears not only in the emission of individual atoms but also in the interaction between them via the field [see Fig. 1(c)]. In this case, the effect of chirality in emission of the two atoms occurs at two levels: in emission of the individual atoms and the in cooperation between them.

In order to proceed further, we write

$$\gamma_{ij} = \gamma_{ij}^{(g)} + \gamma_{ij}^{(r)},$$
$$\Omega_{ij} = \Omega_{ij}^{(g)} + \Omega_{ij}^{(r)}, \tag{18}$$

where the pair of $\gamma_{ij}^{(g)}$ and $\Omega_{ij}^{(g)}$ and the pair of $\gamma_{ij}^{(r)}$ and $\Omega_{ij}^{(r)}$ describe the contributions from guided and radiation modes, respectively. The coefficients $\gamma_{ij}^{(g)}$ and $\gamma_{ij}^{(r)}$ are given by

$$\gamma_{ij}^{(g)} = 2\pi \sum_{fl} G_{\mu_0 i} G_{\mu_0 j}^*,$$
$$\gamma_{ij}^{(r)} = 2\pi \int_{-k_0}^{k_0} d\beta \sum_{ml} G_{\nu_0 i} G_{\nu_0 j}^*, \tag{19}$$

where $\mu_0 = (\omega_0, f, l)$ and $\nu_0 = (\omega_0, \beta, m, l)$ label the resonant guided and radiation modes, whose frequencies coincide with the atomic frequency ω_0. The coefficients $\Omega_{ij}^{(g)}$ and $\Omega_{ij}^{(r)}$ are given by

$$\Omega_{ij}^{(g)} = -\mathrm{P} \int_0^\infty d\omega \sum_{fl} \left[\frac{G_{\omega fli} G_{\omega flj}^*}{\omega - \omega_0} + (-1)^{\delta_{ij}} \frac{\tilde{G}_{\omega fli}^* \tilde{G}_{\omega flj}}{\omega + \omega_0} \right],$$

$$\Omega_{ij}^{(r)} = -\mathrm{P} \int_0^\infty d\omega \sum_{ml} \int_{-k}^{k} d\beta \left[\frac{G_{\omega\beta mli} G_{\omega\beta mlj}^*}{\omega - \omega_0} \right.$$
$$\left. + (-1)^{\delta_{ij}} \frac{\tilde{G}_{\omega\beta mli}^* \tilde{G}_{\omega\beta mlj}}{\omega + \omega_0} \right]. \tag{20}$$

The directional components $\gamma_{ij}^{(g)f}$ of the decay rate coefficients $\gamma_{ij}^{(g)}$ for guided modes are given as

$$\gamma_{ij}^{(g)f} = 2\pi \sum_l G_{\omega_0 fli} G_{\omega_0 flj}^*. \tag{21}$$

The directional components $\gamma_{ij}^{(r)\pm}$ of the decay rate coefficients $\gamma_{ij}^{(r)}$ for radiation modes are given as

$$\gamma_{ij}^{(r)+} = 2\pi \int_0^{k_0} d\beta \sum_{ml} G_{\nu_0 i} G_{\nu_0 j}^*,$$

$$\gamma_{ij}^{(r)-} = 2\pi \int_{-k_0}^{0} d\beta \sum_{ml} G_{\nu_0 i} G_{\nu_0 j}^*. \tag{22}$$

We note that, when the atoms are in free space, the decay rate coefficients and the dipole-dipole interaction coefficients are given as [52–54]

$$\gamma_{ij}^{(\text{vac})} = \frac{\omega_0^3}{2\pi\hbar\epsilon_0 c^3} \left\{ [\mathbf{d}_i \mathbf{d}_j^* - 3(\mathbf{d}_i \cdot \hat{\mathbf{R}}_{ij})(\mathbf{d}_j^* \cdot \hat{\mathbf{R}}_{ij})] \right.$$
$$\times \left(\frac{\cos k_0 R_{ij}}{k_0^2 R_{ij}^2} - \frac{\sin k_0 R_{ij}}{k_0^3 R_{ij}^3} \right)$$
$$\left. + [\mathbf{d}_i \mathbf{d}_j^* - (\mathbf{d}_i \cdot \hat{\mathbf{R}}_{ij})(\mathbf{d}_j^* \cdot \hat{\mathbf{R}}_{ij})] \frac{\sin k_0 R_{ij}}{k_0 R_{ij}} \right\} \tag{23}$$

and

$$\Omega_{ij}^{(\text{vac})}\Big|_{i\neq j} = \frac{\omega_0^3}{4\pi\hbar\epsilon_0 c^3} \left\{ [\mathbf{d}_i \mathbf{d}_j^* - 3(\mathbf{d}_i \cdot \hat{\mathbf{R}}_{ij})(\mathbf{d}_j^* \cdot \hat{\mathbf{R}}_{ij})] \right.$$
$$\times \left(\frac{\sin k_0 R_{ij}}{k_0^2 R_{ij}^2} + \frac{\cos k_0 R_{ij}}{k_0^3 R_{ij}^3} \right)$$
$$\left. - [\mathbf{d}_i \mathbf{d}_j^* - (\mathbf{d}_i \cdot \hat{\mathbf{R}}_{ij})(\mathbf{d}_j^* \cdot \hat{\mathbf{R}}_{ij})] \frac{\cos k_0 R_{ij}}{k_0 R_{ij}} \right\}. \tag{24}$$

Here, we have introduced the notation $\hat{\mathbf{R}}_{ij} = \mathbf{R}_{ij}/R_{ij}$ and $R_{ij} = |\mathbf{R}_{ij}|$, where $\mathbf{R}_{ij} = \mathbf{R}_i - \mathbf{R}_j$. According to Eq. (23), the single-atom free-space coefficients $\gamma_{ii}^{(\text{vac})}$ are real. It is clear from Eqs. (23) and (24) that, when the two atoms have the same dipole matrix element, that is, when $\mathbf{d}_1 = \mathbf{d}_2 \equiv \mathbf{d}$, the cross-atom free-space coefficients $\gamma_{12}^{(\text{vac})}$ and $\Omega_{12}^{(\text{vac})}$ are also real. Thus, the interaction between the atoms with the identical dipole matrix element in free space is not chiral. The spatial dependencies of the coefficients $\gamma_{12}^{(\text{vac})}$ and $\Omega_{12}^{(\text{vac})}$ for various orientations of the atomic dipoles have been studied in detail in Refs. [52,53].

B. Dipole-dipole interaction

As already mentioned above, the coefficients Ω_{ij} describe the frequency shifts of the two-atom system. The diagonal coefficients Ω_{jj} describe the shifts of individual atoms. These shifts contain the Lamb shift and the surface-induced potential. The Lamb shift can be formally incorporated into the bare frequency ω_0. When the atoms are not very close to the surface, the surface-induced potential is small. We are not interested in the surface-induced potential in this paper. Therefore, we neglect the diagonal coefficients Ω_{jj}. The off-diagonal coefficients $\Omega_{ij} = \Omega_{ji}^*$, where $i \neq j$, describe the dipole-dipole interaction between the atoms.

We calculate the coefficient $\Omega_{12} = \Omega_{21}^*$. According to Eqs. (20), we have

$$\Omega_{12}^{(g)} = -P \int_0^\infty d\omega \sum_{fl} \left(\frac{G_{\omega fl1} G_{\omega fl2}^*}{\omega - \omega_0} + \frac{\tilde{G}_{\omega fl1}^* \tilde{G}_{\omega fl2}}{\omega + \omega_0} \right),$$

$$\Omega_{12}^{(r)} = -P \int_0^\infty d\omega \sum_{ml} \int_{-k}^k d\beta \left(\frac{G_{\omega\beta ml1} G_{\omega\beta ml2}^*}{\omega - \omega_0} \right.$$
$$\left. + \frac{\tilde{G}_{\omega\beta ml1}^* \tilde{G}_{\omega\beta ml2}}{\omega + \omega_0} \right). \tag{25}$$

We formally extend the field frequency ω from the region $[0,\infty]$ to the region $[-\infty,\infty]$. For guided modes, we use the definitions $\beta(-\omega) = -\beta(\omega)$ and $\mathbf{e}^{(-\omega,f,-l)} = \mathbf{e}^{(\omega,f,l)*}$. For radiation modes, we use the definition $\mathbf{e}^{(-\omega,-\beta,-m,l)} = \mathbf{e}^{(\omega,\beta,m,l)*}$. These definitions are consistent with the time-reversal symmetry of the Maxwell equations. With the aforementioned definitions, we have $G_{-\omega,f,-l,1} G_{-\omega,f,-l,2}^* = -\tilde{G}_{\omega fl1}^* \tilde{G}_{\omega fl2}$ and $G_{-\omega,-\beta,-m,l,1} G_{-\omega,-\beta,-m,l,2}^* = -\tilde{G}_{\omega\beta ml1}^* \tilde{G}_{\omega\beta ml2}$. Then, Eqs. (25) become

$$\Omega_{12}^{(g)} = -P \int_{-\infty}^\infty d\omega \sum_{fl} \frac{G_{\omega fl1} G_{\omega fl2}^*}{\omega - \omega_0}, \tag{26a}$$

$$\Omega_{12}^{(r)} = -P \int_{-\infty}^\infty d\omega \sum_{ml} \int_{-k}^k d\beta \frac{G_{\omega\beta ml1} G_{\omega\beta ml2}^*}{\omega - \omega_0}. \tag{26b}$$

In the case of the waveguide bath models considered in Refs. [40–42,45], the radiation modes are not taken into account, a single polarization of guided modes is considered, and the coupling coefficient $G_{\omega flj}$ for guided modes is replaced by $\sqrt{\gamma_f/2\pi}\, e^{if\omega z_j/v_g}$. Here, γ_f is the decay rate into the direction f of the waveguide axis. In this case, the dipole-dipole interaction coefficient is found from Eq. (26a) to be [40–42,45]

$$\Omega_{12}^{(1D)}\big|_{z_1 \neq z_2} = -\frac{1}{2\pi} \sum_f \gamma_f\, P \int_{-\infty}^\infty d\omega \frac{e^{if\omega z_{12}/v_g}}{\omega - \omega_0}. \tag{27}$$

Here, $z_{ij} = z_i - z_j$ is the difference between the axial positions of atoms i and j. When we use the contour integral method to calculate the integral over ω in Eq. (27), we obtain [40–42,45]

$$\Omega_{12}^{(1D)}\big|_{z_1 \neq z_2} = -\frac{i}{2} \sum_f \mathrm{sgn}(f z_{12}) \gamma_f e^{if\omega_0 z_{12}/v_g}. \tag{28}$$

In the case of nanofibers, we can use the contour integral method to calculate approximately the integral over ω in Eq. (26a) for $\Omega_{12}^{(g)}$. For this purpose, we need to choose an appropriate close contour consisting of the line segments $(-R, \omega_0 - \epsilon)$ and $(\omega_0 + \epsilon, R)$ and two semicircles C_ϵ and C_R connecting the point $\omega_0 - \epsilon$ with the point $\omega_0 + \epsilon$ and the point R with the point $-R$, respectively. Here, $\epsilon > 0$ is a small real number and $R > 0$ is a large real number. The semicircle C_R lies in the upper or lower half plane of ω depending on the asymptotic behavior of the integral kernel $G_{\omega fl1} G_{\omega fl2}^*$. According to Eq. (7), the product $G_{\omega fl1} G_{\omega fl2}^*$ contains the factor $e^{if\beta(z_1-z_2)}$. We assume that $z_1 \neq z_2$ and that the ω dependence of $G_{\omega fl1} G_{\omega fl2}^*$ is mainly determined by the

factor $e^{if\beta(z_1-z_2)}$. With an appropriate choice of the half plane to place C_R, we can make the integral over this semicircle vanishing. The integral over the small semicircle C_ϵ can be calculated by using the residue theorem. Then, we find

$$\Omega_{12}^{(g)}\big|_{z_1 \neq z_2} \simeq -\pi i \sum_{fl} \mathrm{sgn}(f z_{12}) G_{\omega_0 fl1} G_{\omega_0 fl2}^*. \tag{29}$$

We can rewrite Eq. (29) in the form [40–42,45]

$$\Omega_{12}^{(g)}\big|_{z_1 \neq z_2} \simeq -\frac{i}{2} \sum_f \mathrm{sgn}(f z_{12}) \gamma_{12}^{(g)f}, \tag{30}$$

where $\gamma_{12}^{(g)f}$ is the cross-atom decay coefficient for the f propagation direction. It is clear that Eq. (30) is in agreement with Eq. (28). We can formally extend Eq. (30) for the case of $z_1 = z_2$ by taking the limit $z_2 \to z_1$ under the condition $z_2 > z_1$.

We note that it is not easy to calculate the integral over ω in Eq. (26b) for $\Omega_{12}^{(r)}$. The reason is that the ω dependence of the integral kernel $G_{\omega\beta ml1} G_{\omega\beta ml2}^*$ is complicated.

C. Photon flux

The mean number of photons in guided modes propagating the direction $f = \pm$ is given by

$$N_{\mathrm{gd}}^{(f)} = \sum_l \int_0^\infty \langle a_{\omega fl}^\dagger a_{\omega fl} \rangle d\omega. \tag{31}$$

The mean number of emitted guided-mode photons, summed up over the propagation directions, is $N_{\mathrm{gd}} = N_{\mathrm{gd}}^{(+)} + N_{\mathrm{gd}}^{(-)}$. The flux of photons emitted into the guided modes in the direction $f = \pm$ is given by

$$P_{\mathrm{gd}}^{(f)} = \dot{N}_{\mathrm{gd}}^{(f)} = \sum_l \int_0^\infty \langle \dot{a}_{\omega fl}^\dagger a_{\omega fl} + a_{\omega fl}^\dagger \dot{a}_{\omega fl} \rangle d\omega. \tag{32}$$

We insert Eqs. (10) and (12) into Eq. (32) and neglect the fast rotating terms. Then, we obtain

$$P_{\mathrm{gd}}^{(f)} = \sum_{ij} \gamma_{ij}^{(g)f} \langle \sigma_i^\dagger \sigma_j \rangle, \tag{33}$$

that is,

$$P_{\mathrm{gd}}^{(f)} = \gamma_{11}^{(g)f} \langle \sigma_1^\dagger \sigma_1 \rangle + \gamma_{22}^{(g)f} \langle \sigma_2^\dagger \sigma_2 \rangle + \gamma_{12}^{(g)f} \langle \sigma_1^\dagger \sigma_2 \rangle + \gamma_{21}^{(g)f} \langle \sigma_2^\dagger \sigma_1 \rangle. \tag{34}$$

In terms of the density matrix ρ, Eq. (34) can be rewritten as

$$P_{\mathrm{gd}}^{(f)} = \gamma_{11}^{(g)f} (\rho_{++,++} + \rho_{+-,+-})$$
$$+ \gamma_{22}^{(g)f} (\rho_{++,++} + \rho_{-+,-+})$$
$$+ \gamma_{12}^{(g)f} \rho_{-+,+-} + \gamma_{21}^{(g)f} \rho_{+-,-+}. \tag{35}$$

The flux $P_{\mathrm{gd}} = P_{\mathrm{gd}}^{(+)} + P_{\mathrm{gd}}^{(-)}$ of photons emitted into guided modes in the two directions $f = \pm$ is given as

$$P_{\mathrm{gd}} = \gamma_{11}^{(g)} (\rho_{++,++} + \rho_{+-,+-}) + \gamma_{22}^{(g)} (\rho_{++,++} + \rho_{-+,-+})$$
$$+ \gamma_{12}^{(g)} \rho_{-+,+-} + \gamma_{21}^{(g)} \rho_{+-,-+}. \tag{36}$$

Similarly, the flux of photons emitted into radiation modes is given by

$$P_{\text{rad}} = \gamma_{11}^{(r)}(\rho_{++,++} + \rho_{+-,+-}) + \gamma_{22}^{(r)}(\rho_{++,++} + \rho_{-+,-+})$$
$$+ \gamma_{12}^{(r)}\rho_{-+,+-} + \gamma_{21}^{(r)}\rho_{+-,-+}. \quad (37)$$

The mean number of photons emitted into radiation modes is $N_{\text{rad}}(t) = \int_{t_0}^{t} P_{\text{rad}}(t')dt'$.

The total flux $P_{\text{tot}} = P_{\text{gd}} + P_{\text{rad}}$ of photons emitted into guided and radiation modes is given as

$$P_{\text{tot}} = \gamma_{11}(\rho_{++,++} + \rho_{+-,+-}) + \gamma_{22}(\rho_{++,++} + \rho_{-+,-+})$$
$$+ \gamma_{12}\rho_{-+,+-} + \gamma_{21}\rho_{+-,-+}. \quad (38)$$

The mean number of photons emitted into guided and radiation modes is $N_{\text{tot}}(t) = \int_{t_0}^{t} P_{\text{tot}}(t')dt'$. It can be shown that

$$P_{\text{tot}} = -\dot{\rho}_{\text{exc}}, \quad (39)$$

where $\rho_{\text{exc}} = \rho_{\text{exc}}^{(1)} + \rho_{\text{exc}}^{(2)}$ with $\rho_{\text{exc}}^{(j)} = \langle\sigma_j^{\dagger}\sigma_j\rangle$ being the population of the excited level of atom j.

It is clear that the coefficients of the terms in the expressions for the photon fluxes are the single- and cross-atom decay coefficients. The dipole-dipole interaction coefficients do not enter these expressions explicitly.

IV. NUMERICAL CALCULATIONS

In what follows, we present the results of our numerical calculations pertaining to the decay rate coefficients, the dipole-dipole interaction coefficients, the time dependencies of the populations of the atomic excited states, and the fluxes and mean numbers of emitted guided-mode photons. Since the case of real dipole matrix elements has been studied [26], we consider here the case where the dipole matrix elements are complex vectors. In this case, spontaneous emission and scattering of light may become asymmetric with respect to the opposite axial propagation directions [27–32]. The directionality of emission from a single atom occurs when the atomic dipole matrix element vector is a complex vector in the plane that contains the fiber axis and the atomic position [27]. To be specific, we assume that the atomic transitions are σ_+ transitions with respect to the y axis, that is, the dipole matrix elements of the atoms are $\mathbf{d}_j = (d/\sqrt{2})(i,0,-1)$ for $j = 1,2$.

The experimental technique for the preparation of a linear array of atoms with $\sigma_{\pm}$ transitions in a nanofiber-based trap has been described in Ref. [29]. This technique is based on the use of optical pumping, microwave π pulses, and a fictitious magnetic field to selectively excite a linear array of trapped cesium atoms on one side of the fiber to one of the outermost Zeeman states $|F' = 5, M' = \pm 5\rangle$ of the hyperfine level $6P_{3/2}F' = 5$ of the excited state $6P_{3/2}$. On decay from the Zeeman state $|F' = 5, M' = 5\rangle$ or $|F' = 5, M' = -5\rangle$, due to the selection rules, the atom can make only the σ_+ or σ_- transition, respectively, to the Zeeman state $|F = 4, M = 4\rangle$ or $|F = 4, M = -4\rangle$, respectively, of the hyperfine level $6S_{1/2}F = 4$ of the ground state $6S_{1/2}$.

Regarding optical pumping to transfer the atomic population to the state $|F = 4, M = 4\rangle$ or $|F = 4, M = -4\rangle$, one might be concerned by the fact that the polarization of the evanescent field at the position of the atom on the x axis is not perfectly circular in the zx plane when a x-polarized guided field is used for optical pumping. However, optical pumping can still work very well in this situation because the wrong polarization component only couples weakly to the atom due to the 45/1 ratio of the corresponding transition strengths. In addition, the wrong polarization component is small compared to the right polarization component. Alternatively, one can always use an external circularly polarized light field that propagates along the y axis in order to implement optical pumping, thereby circumventing any imperfection in the preparation of the state $|F = 4, M = 4\rangle$ or $|F = 4, M = -4\rangle$.

One might also be concerned by the fact that, if an x-polarized guided field is used to excite the state $|F' = 5, M' = 5\rangle$ or $|F' = 5, M' = -5\rangle$ from the state $|F = 4, M = 4\rangle$ or $|F = 4, M = -4\rangle$, respectively, this field drives not only the desired transition but also the undesired transition $|F = 4, M = 4\rangle \rightarrow |F' = 5, M' = 3\rangle$ or $|F = 4, M = -4\rangle \rightarrow |F' = 5, M' = -3\rangle$, respectively. However, the wrong transition is strongly suppressed due to the 45/1 ratio of the corresponding transition strengths. In addition, the excitation field component with the wrong polarization is small compared to the component with the right polarization. Moreover, one can always apply a real offset magnetic field that detunes the undesired transition and, thus, further suppresses the undesired coupling. Alternatively, one can also use an external circularly polarized light field that propagates along the y axis in order to excite the state $|F' = 5, M' = 5\rangle$ or $|F' = 5, M' = -5\rangle$.

We emphasize that the assumption of the σ_+ transition concerns only the atoms but not the nanofiber modes. Indeed, the real polarization of the nanofiber modes is used in our calculations, and consequently, an atom with the σ_+ transition can emit a photon not only in the direction $f = +$ but also in the direction $f = -$.

In our numerical calculations, we take the fiber radius $a = 250$ nm and the wavelength of the atomic transition $\lambda_0 = 852$ nm. The refractive indices of the fiber and the surrounding vacuum are $n_1 = 1.45$ and $n_2 = 1$, respectively. The single- and cross-atom decay coefficients will be compared to the decay rate $\gamma_0 = \omega_0^3 d^2/(3\pi\hbar\epsilon_0 c^3)$ of a single atom in free space.

A. Decay rate coefficients

We calculate the single-atom decay rates $\gamma_{jj}^{(g)}$ and $\gamma_{jj}^{(r)}$ into guided and radiation modes, respectively, and the cross-atom decay coefficients $\gamma_{12}^{(g)}$ and $\gamma_{12}^{(r)}$ into guided and radiation modes, respectively, as functions of the radial and axial positions of the atoms. We plot the single-atom decay rates $\gamma_{jj}^{(g)}$ and $\gamma_{jj}^{(r)}$ in Figs. 2 and 3, respectively. We plot the absolute values of the cross-atom decay coefficients $\gamma_{12}^{(g)}$ and $\gamma_{12}^{(r)}$ in Figs. 4 and 5, respectively. We also plot the directional components $\gamma_{jj}^{(g)f}$ and $\gamma_{jj}^{(r)f}$ of the rates $\gamma_{jj}^{(g)}$ and $\gamma_{jj}^{(r)}$, respectively, in Figs. 2 and 3, respectively, and the absolute values of the directional components $\gamma_{12}^{(g)f}$ and $\gamma_{12}^{(r)f}$ of the rate coefficients $\gamma_{12}^{(g)}$ and $\gamma_{12}^{(r)}$, respectively, in Figs. 4 and 5, respectively. Parts (a) and (b) of Figs. 2–5 stand for the dependencies of the rate coefficients on the radial and axial positions of the atoms, respectively. The dotted blue, dashed
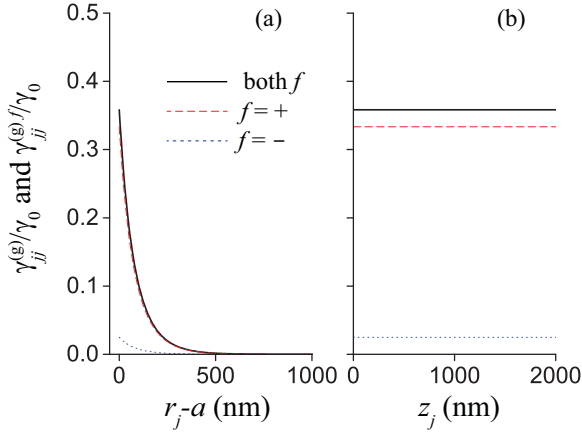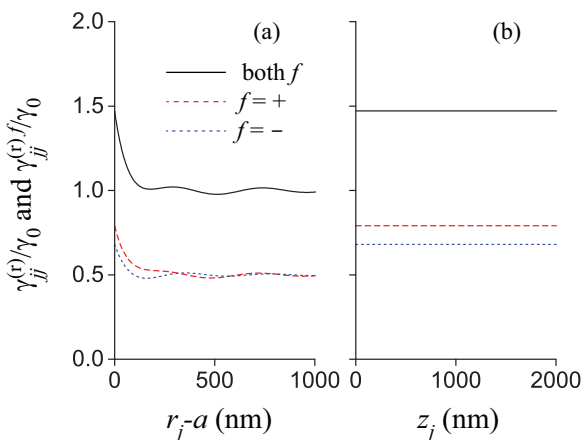
FIG. 2. Decay rate $\gamma_{jj}^{(g)}$ into guided modes (solid black lines) and its directional components $\gamma_{jj}^{(g)f}$ for $f = +$ (dashed red lines) and $f = -$ (dotted blue lines), relative to the free-space spontaneous decay rate γ_0, as functions of (a) the radial position $r_j - a$ and (b) the axial position z_j of atom j. One coordinate of the atom is varied, while the two others are fixed as (a) $\varphi_j = 0$ and $z_j = 0$ and (b) $r_j = a$ and $\varphi_j = 0$. The dipole matrix element of the atom is $\mathbf{d}_j = (d/\sqrt{2})(i, 0, -1)$, corresponding to the σ_+-polarized transition with respect to the y quantization axis. The fiber radius is $a = 250$ nm. The refractive indices of the fiber and the surrounding vacuum are $n_1 = 1.45$ and $n_2 = 1$, respectively. The wavelength of the atomic transition is $\lambda_0 = 852$ nm.

red, and solid black curves refer to the rate coefficients for the negative ($f = -$) direction, the positive ($f = +$) direction, and the sum of the rate coefficients for the two opposite directions, respectively. Comparison between the dashed red and dotted blue curves shows that the rate coefficients are different for the opposite axial directions $f = +$ and $f = -$. As already mentioned, the asymmetry is due to the existence of a nonzero longitudinal component of the nanofiber field, which is in phase quadrature with respect to the radial transverse component [27–32]. This asymmetry occurs when

the ellipticity vector of the atomic dipole polarization overlaps with the ellipticity vector of the field polarization [27,47]. The directional spontaneous emission is a signature of spin-orbit coupling of light carrying transverse spin angular momentum [33–38]. We observe from Fig. 2(a) that, for the parameters of the figure, we have $\gamma_{jj}^{(g)+} > \gamma_{jj}^{(g)-}$, that is, spontaneous emission into guided modes in the positive direction $f = +$ is stronger than that in the negative direction $f = -$. The dominance of spontaneous emission into guided modes in the direction $f = +$ occurs for any radial distance r in the case
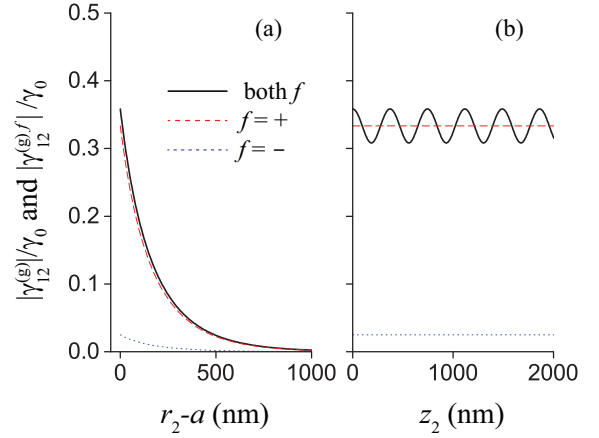

FIG. 4. Absolute value $|\gamma_{12}^{(g)}|$ of the coefficient of the cross-atom decay into guided modes (solid black lines) and its directional components $|\gamma_{12}^{(g)f}|$ for $f = +$ (dashed red lines) and $f = -$ (dotted blue lines), relative to the free-space spontaneous decay rate γ_0, as functions of (a) the radial position $r_2 - a$ and (b) the axial position z_2 of atom 2. The position of atom 1 is fixed at $r_1 = a$, $\varphi_1 = 0$, and $z_1 = 0$. One coordinate of atom 2 is varied, while the two others are fixed as (a) $\varphi_2 = 0$ and $z_2 = 0$ and (b) $r_2 = a$ and $\varphi_2 = 0$. The dipole matrix elements of both atoms are $\mathbf{d}_1 = \mathbf{d}_2 = (d/\sqrt{2})(i, 0, -1)$, corresponding to the σ_+-polarized transitions with respect to the y quantization axis. Other parameters are as for Fig. 2.

FIG. 3. Decay rate $\gamma_{jj}^{(r)}$ into radiation modes (solid black lines) and its directional components $\gamma_{jj}^{(r)f}$ for $f = +$ (dashed red lines) and $f = -$ (dotted blue lines), relative to the free-space spontaneous decay rate γ_0, as functions of (a) the radial position $r_j - a$ and (b) the axial position z_j of atom j. Other parameters are as for Fig. 2.
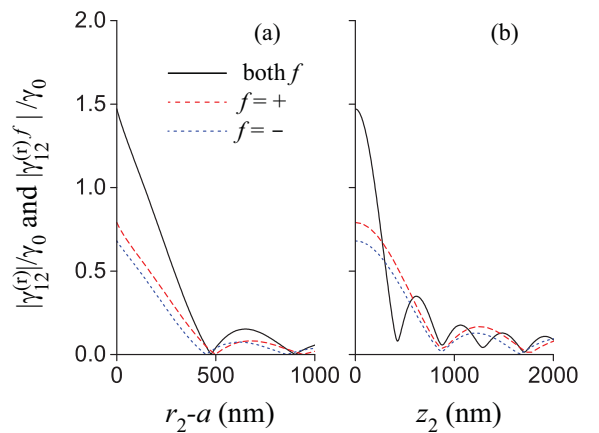

FIG. 5. Absolute value $|\gamma_{12}^{(r)}|$ of the coefficient of the cross-atom decay into radiation modes (solid black lines) and its directional components $|\gamma_{12}^{(r)f}|$ for $f = +$ (dashed red lines) and $f = -$ (dotted blue lines), relative to the free-space spontaneous decay rate γ_0, as functions of (a) the radial position $r_2 - a$ and (b) the axial position z_2 of atom 2. Other parameters are as for Figs. 2 and 4.

considered. Meanwhile, Fig. 3(a) shows that, in spontaneous emission into radiation modes, both the possibilities $\gamma_{jj}^{(r)+} > \gamma_{jj}^{(r)-}$ and $\gamma_{jj}^{(r)+} < \gamma_{jj}^{(r)-}$ may appear, depending on the radial distance r [31]. The dependencies of the rate coefficients $\gamma_{jj}^{(r)f}$ and $\gamma_{12}^{(r)f}$ for radiation modes (see Figs. 3 and 5) on the emission direction f are, in general, weaker than those of the rate coefficients $\gamma_{jj}^{(g)f}$ and $\gamma_{12}^{(g)f}$ for guided modes (see Figs. 2 and 4), respectively. Careful inspection of Figs. 2 and 3 shows that the sum of the single-atom decay rates for the positive direction $f = +$ and the negative direction $f = -$ gives the total single-atom decay rate for the two directions. Since the cross-atom decay coefficients are complex parameters, the sum of the absolute values of the cross-atom decay coefficients for $f = +$ and $f = -$ may be different from the absolute value of the total cross-atom decay coefficient for the two directions [see Figs. 4(b) and 5(b)].

The results presented in Figs. 2 and 3 are in perfect agreement with the results of Refs. [27,31]. The steep reductions of the decay rate coefficients $\gamma_{jj}^{(g)}$ and $\gamma_{12}^{(g)}$ with increasing radial distance in Figs. 2(a) and 4(a), respectively, are the consequences of the evanescent-wave nature of the field in the guided modes. The single-atom decay rates $\gamma_{jj}^{(g)}$ and $\gamma_{jj}^{(r)}$ do not depend on the axial position z_j [see Figs. 2(b) and 3(b)]. Meanwhile, the cross-atom decay coefficients $\gamma_{12}^{(g)}$ and $\gamma_{12}^{(r)}$ oscillate with increasing axial separation between the atoms [see Figs. 4(b) and 5(b)]. It can be easily discerned from Figs. 4(b) and 5(b) that the effect of guided modes on the cross-atom decay persists over arbitrarily large axial separations between the atoms while that due to the radiation modes decays to zero. Thus, the guided modes of the fiber play a crucial role in maintaining the coupling over large distances [26]. It is clear that one can control the coupling between the atoms by varying the separation between them with maximum coupling at certain locations. We observe from Fig. 4(b) that the cross-atom guided-mode-mediated decay coefficient $\gamma_{12}^{(g)}$ oscillates with increasing axial separation but does not cross the zero value axis. This behavior is a consequence of chiral coupling between the atoms. Indeed, in the case considered, we have $|\gamma_{12}^{(g)+}| > |\gamma_{12}^{(g)-}|$. Meanwhile, $\gamma_{12}^{(g)+}$ and $\gamma_{12}^{(g)-}$ are complex parameters, whose dependencies on the axial coordinates of the atoms are given by the factors $\exp(i\beta_0 z_{12})$ and $\exp(-i\beta_0 z_{12})$, respectively. Since $|\gamma_{12}^{(g)+}| > |\gamma_{12}^{(g)-}|$, the interference between $\gamma_{12}^{(g)+}$ and $\gamma_{12}^{(g)-}$ can never be completely destructive. Thus, in the case of chiral coupling, the cross-atom guided-mode-mediated decay coefficient $\gamma_{12}^{(g)}$ is nonzero for arbitrary values z_{12}. It is worth noting that in the case of nonchiral coupling [26], $\gamma_{12}^{(g)}$ vanishes when $\beta_0 z = \pi/2 + n\pi$, where $n = 0, 1, 2, \dots$.

As already mentioned, in the case where the dipole matrix elements $\mathbf{d}_j$ are complex vectors, the cross-atom decay coefficients $\gamma_{12}^{(g)}$ and $\gamma_{12}^{(r)}$ into guided and radiation modes, respectively, are, in general, complex parameters. In order to illustrate this feature, we plot separately the real and imaginary parts of $\gamma_{12}^{(g)}$ in Fig. 6 and the real and imaginary parts of $\gamma_{12}^{(r)}$ in Fig. 7. In addition, we plot in Fig. 8 the absolute value $|\gamma_{12}|$ and the phase φ_{12} of the total cross-atom decay coefficient
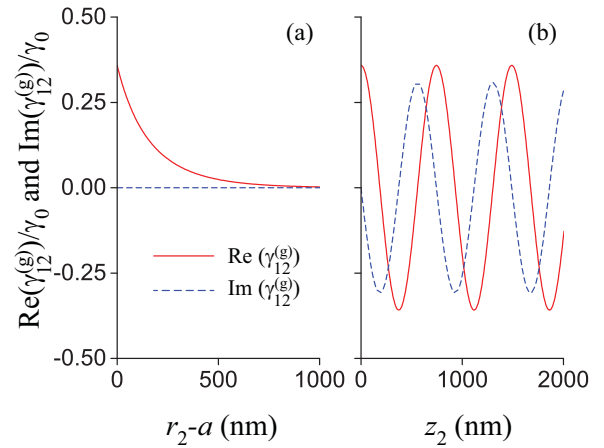

FIG. 6. Real (solid red lines) and imaginary (dashed blue lines) parts of the coefficient $\gamma_{12}^{(g)}$ for cross-atom decay into guided modes, relative to the free-space spontaneous decay rate γ_0, as functions of (a) the radial position $r_2 - a$ and (b) the axial position z_2 of atom 2. Other parameters are as for Figs. 2 and 4.

$\gamma_{12} = \gamma_{12}^{(g)} + \gamma_{12}^{(r)}$. Figures 6(a) and 6(b) show, respectively, the evanescent-wave behavior of the radial dependence and the oscillatory behavior of the axial dependence of the cross-atom coefficient $\gamma_{12}^{(g)}$ of decay into guided modes. We observe from Fig. 6(b) that the real and imaginary parts of $\gamma_{12}^{(g)}$ oscillate periodically with different phases along the fiber axis. Figure 7 shows that the cross-atom coefficient $\gamma_{12}^{(r)}$ of decay into radiation modes oscillates in the radial and axial directions and that the amplitude of oscillations reduces with increasing separation between the atoms. Figure 8(a) indicates the possibility of the channels of decay into guided and radiation modes to act out of phase, leading to $\gamma_{12} = 0$ at certain points. We observe from Figs. 8(c) and 8(d) that the
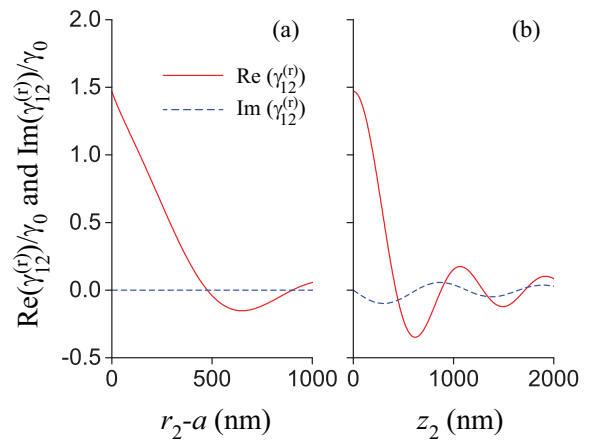

FIG. 7. Real (solid red lines) and imaginary (dashed blue lines) parts of the coefficient $\gamma_{12}^{(r)}$ for cross-atom decay into radiation modes, relative to the free-space spontaneous decay rate γ_0, as functions of (a) the radial position $r_2 - a$ and (b) the axial position z_2 of atom 2. Other parameters are as for Figs. 2 and 4.
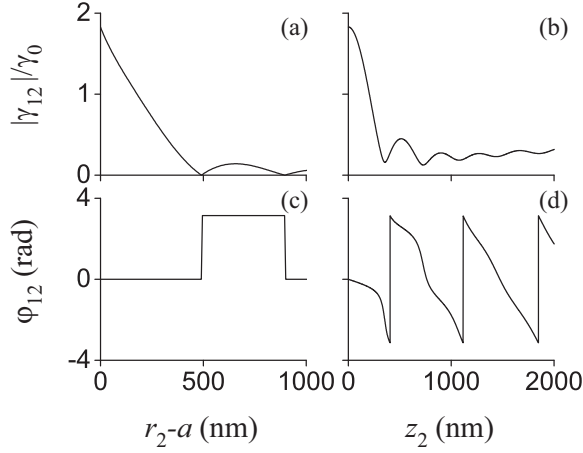
FIG. 8. Absolute value $|\gamma_{12}|$ (top row) and phase φ_{12} (bottom row) of the total cross-atom decay coefficient γ_{12} as functions of the radial position $r_2 - a$ (left column) and the axial position z_2 (right column) of atom 2. Other parameters are as for Figs. 2 and 4.

phase φ_{12} of the total cross-atom decay coefficient γ_{12} depends on the positions of the atoms.

B. Dipole-dipole interaction coefficients

We plot in Fig. 9 the real and imaginary parts of the guided-mode-mediated dipole-dipole interaction coefficient $\Omega_{12}^{(g)}$. Figures 9(a) and 9(b) show, respectively, the evanescent-wave behavior of the radial dependence and the oscillatory behavior of the axial dependence of the coefficient $\Omega_{12}^{(g)}$. We observe from Fig. 9(b) that the real and imaginary parts of $\Omega_{12}^{(g)}$ oscillate periodically with different phases along the fiber axis.

The expression (26b) for the radiation-mode-mediated dipole-dipole interaction coefficient $\Omega_{12}^{(r)}$ contains a double
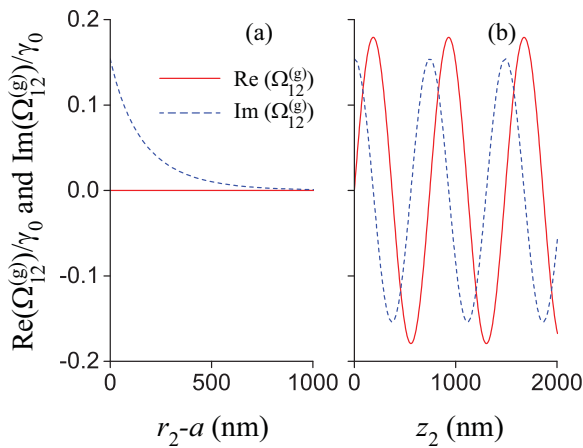
FIG. 9. Real (solid red lines) and imaginary (dashed blue lines) parts of the guided-mode-mediated dipole-dipole interaction coefficient $\Omega_{12}^{(g)}$, relative to the free-space spontaneous decay rate γ_0, as functions of (a) the radial position $r_2 - a$ and (b) the axial position z_2 of atom 2. Parameters used are as for Figs. 2 and 4. In (a), we formally take the limit $z_2 \to z_1$ under the condition $z_2 > z_1$.

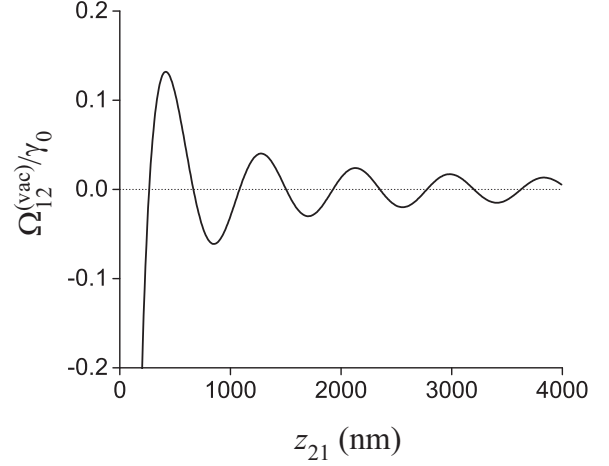FIG. 10. Free-space dipole-dipole interaction coefficient $\Omega_{12}^{(\mathrm{vac})}$, relative to the free-space spontaneous decay rate γ_0, as a function of the distance $z_{21} = z_2 - z_1$ between the atoms along the axis z. The other coordinates of the atoms are $r_1 = r_2$ and $\varphi_1 = \varphi_2$. The dipole matrix elements of the atoms are $\mathbf{d}_1 = \mathbf{d}_2 = (d/\sqrt{2})(i, 0, -1)$, corresponding to the σ_+-polarized transitions with respect to the y quantization axis. The dotted line is the zero horizontal axis and is a guide to the eye.

integral and a double sum of Bessel functions. It is not easy to calculate numerically this coefficient. When the atoms are not too close to the fiber surface, the effect of the fiber on $\Omega_{12}^{(r)}$ is not serious. In this case, $\Omega_{12}^{(r)}$ is close to $\Omega_{12}^{(\mathrm{vac})}$, where $\Omega_{12}^{(\mathrm{vac})}$ is the dipole-dipole interaction coefficient for atoms in free-space. We use the approximation $\Omega_{12}^{(r)} \simeq \Omega_{12}^{(\mathrm{vac})} \sqrt{\gamma_{11}^{(r)} \gamma_{22}^{(r)}}/\gamma_0$. Here, we have added the factor $\sqrt{\gamma_{11}^{(r)} \gamma_{22}^{(r)}}/\gamma_0$ to take into account the effect of the fiber on the mode density of radiation modes. As already mentioned in the previous section, the free-space dipole-dipole interaction coefficient $\Omega_{12}^{(\mathrm{vac})}$ is real in the case where the two atoms have the same dipole matrix element ($\mathbf{d}_1 = \mathbf{d}_2 \equiv \mathbf{d}$). We plot in Fig. 10 the coefficient $\Omega_{12}^{(\mathrm{vac})}$ as a function of the distance between the atoms. We depict in Fig. 11 the absolute value $|\Omega_{12}|$ and the phase θ_{12} of the total dipole-dipole interaction coefficient $\Omega_{12} = \Omega_{12}^{(g)} + \Omega_{12}^{(r)}$. Figure 10 shows that the free-space dipole-dipole interaction coefficient $\Omega_{12}^{(\mathrm{vac})}$ oscillates and decays with increasing separation between the atoms. Figure 11(a) indicates that Ω_{12} becomes close to zero at certain positions of the atoms along the radial direction. This feature is due to the existence of zeros of $\Omega_{12}^{(\mathrm{vac})}$ (see Fig. 10) and the quick reduction of $\Omega_{12}^{(g)}$ with increasing distance of one of the atoms to the fiber surface. We observe from Figs. 11(c) and 11(d) that the phase θ_{12} of the total dipole-dipole interaction coefficient Ω_{12} depends on the positions of the atoms. Comparison between Figs. 8(c) and 11(c) and between Figs. 8(d) and 11(d) shows that the phases φ_{12} and θ_{12} of the coefficients γ_{12} and Ω_{12} are, in general, different from each other.

C. Dynamics

We solve the master equation (16) for different initial states. We use the solutions of this equation to calculate
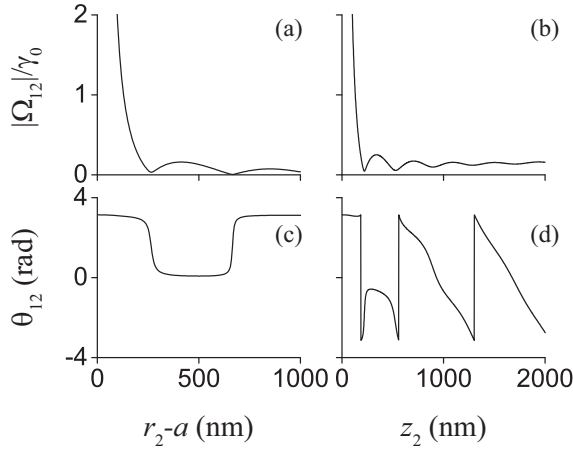
FIG. 11. Absolute value $|\Omega_{12}|$ (top row) and phase θ_{12} (bottom row) of the total dipole-dipole interaction coefficient Ω_{12} as functions of the radial position $r_2 - a$ (left column) and the axial position z_2 (right column) of atom 2. Other parameters are as for Figs. 2 and 4.

the populations $\rho_{\mathrm{exc}}^{(j)} = \langle \sigma_j^\dagger \sigma_j \rangle$ of the upper levels of atoms $j = 1, 2$, the fluxes $P_{\mathrm{gd}}^{(f)}$ of photons emitted into guided modes in the direction $f = \pm$ along the fiber axis, and the mean number $N_{\mathrm{gd}}^{(f)}$ of photons emitted into guided modes in the direction f. We also calculate the total flux $P_{\mathrm{gd}} = \sum_f P_{\mathrm{gd}}^{(f)}$ and the total mean number $N_{\mathrm{gd}} = \sum_f N_{\mathrm{gd}}^{(f)}$ of photons emitted into guided modes. We study first the cases where an atom is initially excited and the other atom is initially in the ground state and then the cases where the two atoms are prepared in a symmetric or antisymmetric superposition state.

1. An excited atom in the presence of a ground-state atom

We first study the cases where an atom is initially excited and the other atom is initially not excited. In these cases, the initial state of the two-system is $|\psi(0)\rangle = |\psi_1\rangle$ or $|\psi_2\rangle$, where $|\psi_1\rangle \equiv |+-\rangle$ and $|\psi_2\rangle \equiv |-+\rangle$. The direction of radiative transfer in the case of the initial state $|\psi_1\rangle$ or $|\psi_2\rangle$ is from atom 1 to atom 2 or from atom 2 to atom 1, respectively.

We plot in Figs. 12–14 the results of numerical calculations for the case where the coordinates of the atoms are $r_1 - a = r_2 - a = 200$ nm, $\varphi_1 = \varphi_2 = 0$, and $z_2 - z_1 = 150$ nm. Figure 12 shows the time evolution of the populations $\rho_{\mathrm{exc}}^{(j)}$ of the excited states of the atoms in the cases where the initial state of the two-atom system is $|\psi(0)\rangle = |\psi_1\rangle$ (solid red lines) or $|\psi_2\rangle$ (dashed blue lines). We observe in both cases that a part of the atomic excitation is transferred from the excited atom to the ground-state atom, and then is slowly released by emission. Comparison between the solid red and dashed blue lines of Fig. 12 shows that, except for the changes of the roles of the atoms, the differences between the results for the cases of the initial states $|\psi(0)\rangle = |\psi_1\rangle$ and $|\psi(0)\rangle = |\psi_2\rangle$ are very small. Comparison between the solid red line of Fig. 12(a) and the dashed blue line of Fig. 12(b) shows that the decay of $\rho_{\mathrm{exc}}^{(1)}$ in the case of $|\psi(0)\rangle = |\psi_1\rangle$ is almost the same as the decay of $\rho_{\mathrm{exc}}^{(2)}$ in the case of $|\psi(0)\rangle = |\psi_2\rangle$. Meanwhile, a close inspection shows that the peak of the transferred excitation $\rho_{\mathrm{exc}}^{(2)}$ in Fig. 12(b) (see the solid red line of this figure) is
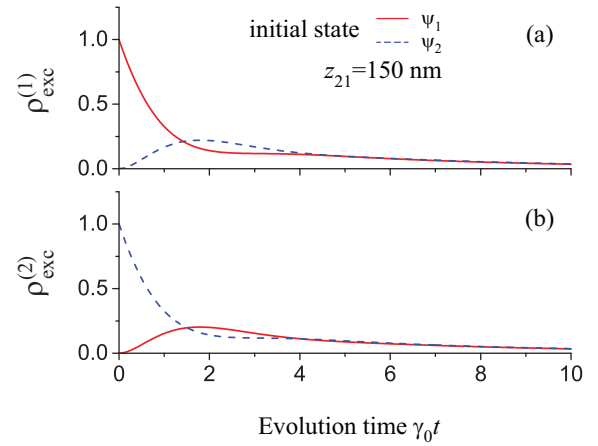

FIG. 12. Time evolution of the populations (a) $\rho_{\mathrm{exc}}^{(1)}$ and (b) $\rho_{\mathrm{exc}}^{(2)}$ of the upper levels of atoms 1 and 2, respectively, in the cases where the initial state of the two-atom system is $|\psi(0)\rangle = |\psi_1\rangle$ (solid red lines) or $|\psi_2\rangle$ (dashed blue lines). The coordinates of the atoms are $r_1 - a = r_2 - a = 200$ nm, $\varphi_1 = \varphi_2 = 0$, and $z_2 - z_1 = 150$ nm. The dipole matrix elements of the atoms are $\mathbf{d}_1 = \mathbf{d}_2 = (d/\sqrt{2})(i, 0, -1)$, corresponding to σ_+-polarized transitions with respect to the y quantization axis. Other parameters are as for Figs. 2 and 4.

slightly different from the peak of the transferred excitation $\rho_{\mathrm{exc}}^{(1)}$ in Fig. 12(a) (see the dashed blue line of this figure). Our additional calculations, which are not shown here, indicate that, depending on the parameters of the system, the peak of the transferred excitation $\rho_{\mathrm{exc}}^{(2)}$ in the case of the initial state $|\psi_1\rangle$ [see the solid red line of Fig. 12(b)] may be slightly larger or smaller than the peak of the transferred excitation $\rho_{\mathrm{exc}}^{(1)}$ in the case of the initial state $|\psi_2\rangle$ [see the dashed blue line of Fig. 12(a)].
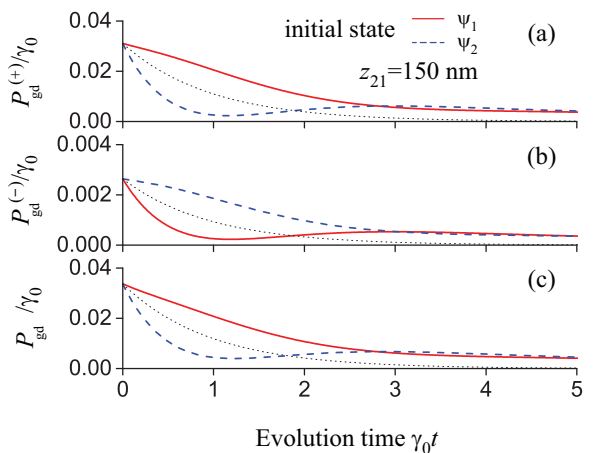

FIG. 13. Time evolution of the photon fluxes (a) $P_{\mathrm{gd}}^{(+)}$, (b) $P_{\mathrm{gd}}^{(-)}$, and (c) P_{gd} in the cases where the initial state of the two-atom system is $|\psi(0)\rangle = |\psi_1\rangle$ (solid red lines) or $|\psi_2\rangle$ (dashed blue lines). Other parameters are as for Figs. 2, 4, and 12. The fluxes are normalized to the decay rate γ_0 of a single atom in free space. For comparison, the results for the case of a single excited atom are shown by the dotted black lines.
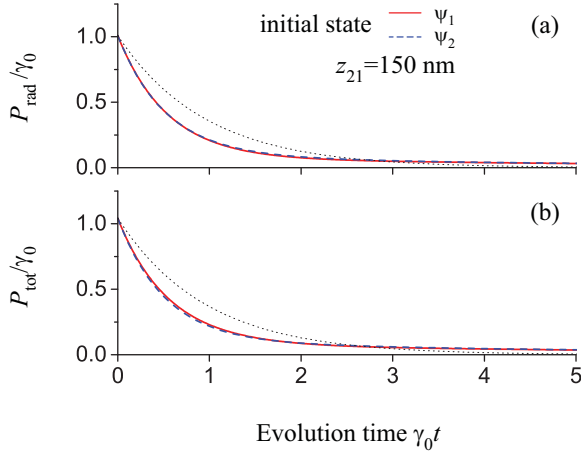
FIG. 14. Time evolution of the photon fluxes (a) $P_{\rm rad}$ and (b) $P_{\rm tot}$ in the cases where the initial state of the two-atom system is $|\psi(0)\rangle = |\psi_1\rangle$ (solid red lines) or $|\psi_2\rangle$ (dashed blue lines). Other parameters are as for Figs. 2, 4, and 12. The fluxes are normalized to the decay rate γ_0 of a single atom in free space. The dotted black lines are for the case of a single excited atom.

Figure 13 shows the time evolution of the fluxes $P_{\rm gd}^{(+)}$ and $P_{\rm gd}^{(-)}$ of photons emitted into guided modes in the positive and negative directions of the fiber axis, respectively, and the total guided-photon flux $P_{\rm gd}$, calculated for the cases where the initial state of the two-atom system is $|\psi(0)\rangle = |\psi_1\rangle$ (solid red lines) or $|\psi_2\rangle$ (dashed blue lines). For comparison, the corresponding results for the case of a single excited atom are shown by the dotted black lines. Comparison between the scales of the vertical axes in Figs. 13(a) and 13(b) shows that the photon flux $P_{\rm gd}^{(+)}$ for the positive direction is about one order larger than the photon flux $P_{\rm gd}^{(-)}$ for the negative direction. Furthermore, we observe that the photon fluxes for the initial states $|\psi_1\rangle$ (solid red lines) and $|\psi_2\rangle$ (dashed blue lines) are substantially different from each other. Thus, the photon fluxes depend on the direction of propagation of light and the direction of radiative transfer between the atoms. We emphasize again that this is a chiral effect and is a signature of spin-orbit coupling of light [33–38]. This effect results from the existence of a nonzero longitudinal component of the nanofiber field, which is in phase quadrature with respect to the radial transverse component [27–32].

Comparison between the solid red, dashed blue, and dotted black lines of Fig. 13 shows that the presence of a ground-state atom in the vicinity of an excited atom may increase or decrease the fluxes of photons emitted into guided modes. Thus, the collective emission into guided modes can be enhanced or suppressed depending on the direction of propagation of light and the direction of radiative transfer between the atoms. We note that the flux of emitted photons depends on not only the single-atom excited populations $\rho_{\rm exc}^{(1)}$ and $\rho_{\rm exc}^{(2)}$ but also on the cross-atom interference. In addition, the atoms can emit not only into guided modes but also into radiation modes.

The variation of the total atomic excitation $\rho_{\rm exc} = \rho_{\rm exc}^{(1)} + \rho_{\rm exc}^{(2)}$ in time is proportional to the total flux $P_{\rm tot}$ of photons emitted into guided and radiation modes [see Eq. (39)]. We

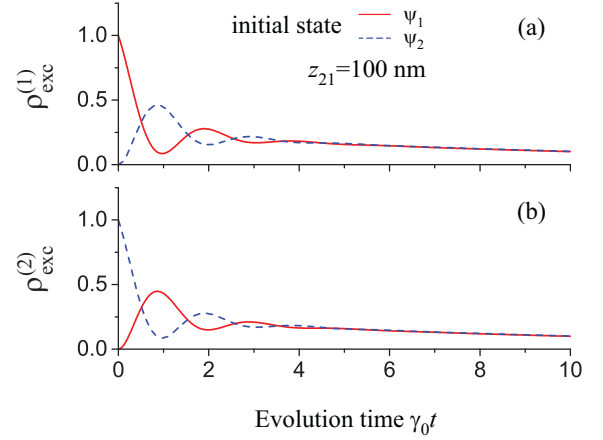FIG. 15. Same as Fig. 12 except for $z_2 - z_1 = 100\,{\rm nm}$.

plot in Fig. 14 the time evolution of the flux $P_{\rm rad}$ of photons emitted into radiation modes and the total photon flux $P_{\rm tot}$ for the parameters of Fig. 13. We observe that, unlike the flux $P_{\rm gd}$ into guides modes, the flux $P_{\rm rad}$ into radiation modes and the total flux $P_{\rm tot}$ do not depend significantly on the direction of excitation transfer. In addition, we observe that, when the interaction time is not zero and not too large, the fluxes $P_{\rm rad}$ and $P_{\rm tot}$ from two atoms in the initial state $|\psi(0)\rangle = |\psi_1\rangle$ (solid red lines) or $|\psi_2\rangle$ (dashed blue lines) are smaller than the corresponding fluxes from a single excited atom (dotted black lines). Such reductions of $P_{\rm rad}$ and $P_{\rm tot}$ are a consequence of the excitation transfer between the atoms. The effect of the cross-atom interference on the fluxes $P_{\rm rad}$ and $P_{\rm tot}$ is not as strong as that on the flux $P_{\rm gd}$.

As already mentioned, when we reduce the distance between the atoms, the dipole-dipole interaction increases. When this interaction is strong enough, we may observe oscillations in the time dependencies of the excited-state populations $\rho_{\rm exc}^{(1)}$ and $\rho_{\rm exc}^{(2)}$ and the photon fluxes $P_{\rm gd}^{(+)}$, $P_{\rm gd}^{(-)}$, and $P_{\rm gd}$. In order to illustrate such a situation, we plot in Figs. 15 and 16 the results of calculations for the quantities presented in Figs. 12 and 13, respectively, using the same parameters except for $z_2 - z_1 = 100\,{\rm nm}$. We observe clearly oscillations in the
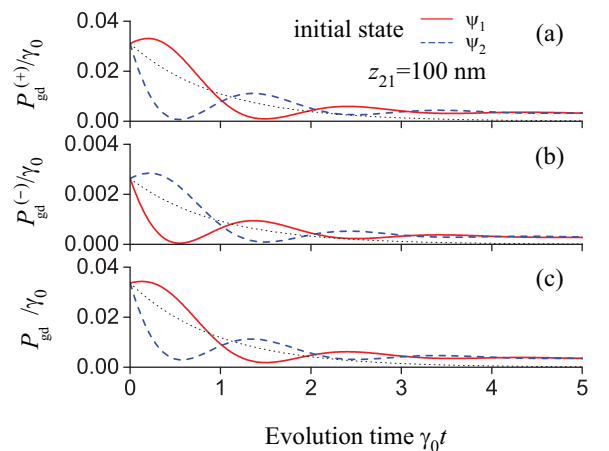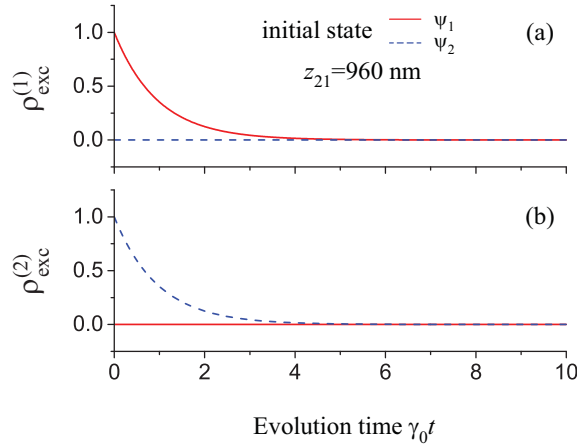

FIG. 16. Same as Fig. 13 except for $z_2 - z_1 = 100\,{\rm nm}$.

FIG. 17. Same as Fig. 12 except for $z_2 - z_1 = 960$ nm.

time evolution of the calculated quantities. For the parameters used, we do not see oscillations in P_{rad} and P_{tot}.

In the limit $z_{21} \to \infty$, the cross-atom radiation-mode-mediated coefficients $\gamma_{12}^{(r)}$ and $\Omega_{12}^{(r)}$ tend to vanish. In this limit, the collective effects are mainly determined by the cross-atom guided-mode-mediated coefficients $\gamma_{12}^{(g)}$ and $\Omega_{12}^{(g)}$, which are, in general, finite. In order to illustrate such a situation, we plot in Figs. 17 and 18 the results of calculations for the quantities presented in Figs. 12 and 13, respectively, using the same parameters except for $z_2 - z_1 = 960$ nm. We observe from Fig. 17 that the transfer of excitation between the atoms is negligible. Figure 18 shows that the differences between the results for the cases $|\psi(0)\rangle = |\psi_1\rangle$ (solid red lines) and $|\psi_2\rangle$ (dashed blue lines) are small but not negligible.

The mean numbers $N_{\text{gd}}^{(+)}$, $N_{\text{gd}}^{(-)}$, and N_{gd} of photons emitted into guided modes in the positive direction, the negative direction, and both directions, respectively, are determined by the integrations of the fluxes $P_{\text{gd}}^{(+)}$, $P_{\text{gd}}^{(-)}$, and P_{gd}, respectively, over the evolution time t. We plot in Figs. 19 and 20 the dependencies of the mean emitted guided photon numbers on the axial atomic separation z_{21} and the atom-to-surface distance $r - a$, respectively. The results for the cases of the initial states $|\psi(0)\rangle = |\psi_1\rangle$ and $|\psi_2\rangle$ are shown by the solid red
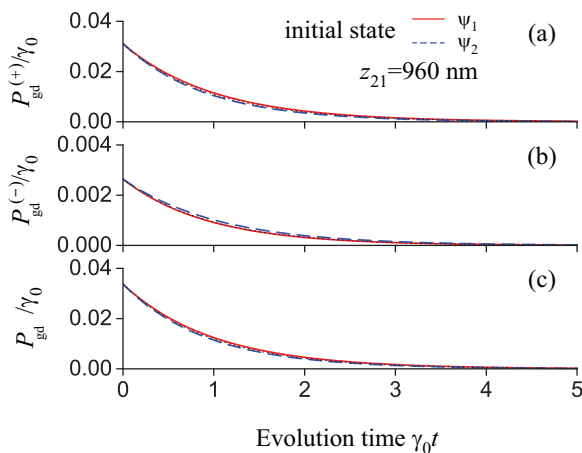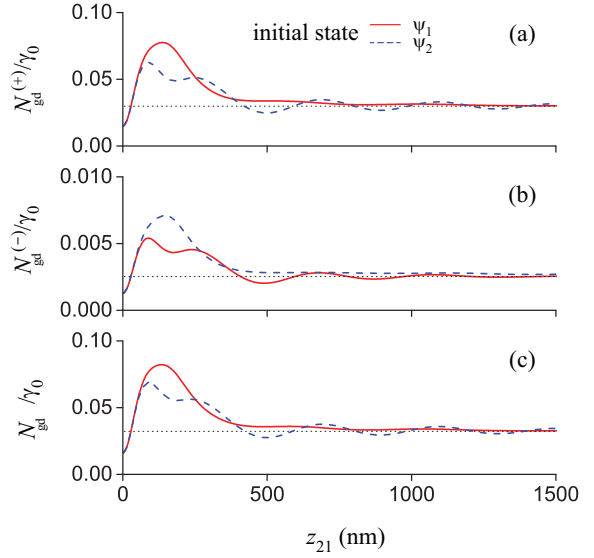

FIG. 19. Dependencies of the mean emitted photon numbers (a) $N_{\text{gd}}^{(+)}$, (b) $N_{\text{gd}}^{(-)}$, and (c) N_{gd} on the axial separation z_{21} between the atoms in the cases where the initial state of the two-atom system is $|\psi(0)\rangle = |\psi_1\rangle$ (solid red lines) or $|\psi_2\rangle$ (dashed blue lines). The radial and azimuthal coordinates of the atoms are $r_1 - a = r_2 - a = 200$ nm and $\varphi_1 = \varphi_2 = 0$, respectively. Other parameters are as for Figs. 2, 4, and 12. The dotted black lines are for the case of a single excited atom.

lines and the dashed blue lines, respectively. For comparison, we plot the corresponding results for the case of a single excited atom by the dotted black lines.

Comparison between the scales of Figs. 19(a) and 19(b) and between the scales of Figs. 20(a) and 20(b) shows that the mean photon number $N_{\text{gd}}^{(+)}$ for the positive direction is about one order larger than the mean photon number $N_{\text{gd}}^{(-)}$ for the negative
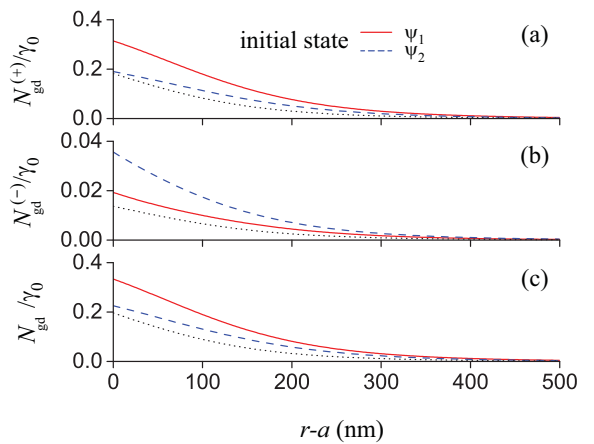

FIG. 18. Same as Fig. 13 except for $z_2 - z_1 = 960$ nm.

FIG. 20. Dependencies of the mean emitted photon numbers (a) $N_{\text{gd}}^{(+)}$, (b) $N_{\text{gd}}^{(-)}$, and (c) N_{gd} on the distance $r - a$ from the atoms to the fiber surface in the cases where the initial state of the two-atom system is $|\psi(0)\rangle = |\psi_1\rangle$ (solid red lines) or $|\psi_2\rangle$ (dashed blue lines). The coordinates of the atoms are $r_1 = r_2 = r$, $\varphi_1 = \varphi_2 = 0$, and $z_2 - z_1 = 150$ nm. Other parameters are as for Figs. 2, 4, and 12. The dotted black lines are for the case of a single excited atom.

direction. It is clear from the figure that the mean emitted guided photon number N_{gd} and its directional components $N_{gd}^{(+)}$ and $N_{gd}^{(-)}$ depend on the axial atomic separation z_{21}, the atom-surface distance $r - a$, and the direction of radiative transfer between the atoms.

When we compare the solid red and dashed blue lines of Fig. 19 with the dotted black lines of this figure, we see that, depending on the axial atomic separation z_{21} and the radiative transfer direction, the presence of a ground-state atom may enhance or suppress the probability for an excited atom to emit a photon into guided modes. In addition, we observe that, depending on z_{21}, the values of $N_{gd}^{(+)}$, $N_{gd}^{(-)}$, and N_{gd} in the case of the initial state $|\psi(0)\rangle = |\psi_1\rangle$ (solid red lines) may be larger or smaller than the corresponding values in the case of the initial state $|\psi(0)\rangle = |\psi_2\rangle$ (dashed blue lines). For z_{21} in the region from 25 to 400 nm, N_{gd} and its directional components $N_{gd}^{(+)}$ and $N_{gd}^{(-)}$ for the two-atom case (see the solid red and dashed blue lines) are significantly larger than the corresponding values for a single excited atom (see the dotted black lines). These differences are signatures of the collective effect in spontaneous emission into guided modes. We note that the total number of emitted photons is fixed as given by the total initial excitation of the atoms. Therefore, an increase or a decrease in the mean number of photons emitted into guided modes is associated with a decrease or an increase, respectively, in the mean number of photons emitted into radiation modes.

The interaction of the atoms prepared in the state $|\psi(0)\rangle = |\psi_1\rangle$ or $|\psi_2\rangle$ with the vacuum of the field may lead to entanglement between the atoms. The entanglement can be characterized by the concurrence C [55]. For two two-level atoms, the density matrix elements are denoted as $\rho_{\alpha\beta}$, where $\alpha, \beta = e, g, a, b$ with $|e\rangle = |++\rangle$, $|g\rangle = |--\rangle$, $|a\rangle = |+-\rangle$, and $|b\rangle = |-+\rangle$. It can be shown from Eq. (16) that, in the case where the matrix elements ρ_{ea}, ρ_{eb}, ρ_{ga}, ρ_{gb} are equal to zero at the initial time, they remain equal to zero for any time. In this case, according to Tanaś and Ficek [56], the concurrence C of the two-atom system is $C = \max(0, C_1, C_2)$, where $C_1 = 2(|\rho_{eg}| - \sqrt{\rho_{aa}\rho_{bb}})$ and $C_2 = 2(|\rho_{ab}| - \sqrt{\rho_{ee}\rho_{gg}})$.

We plot in Fig. 21 the time dependence of the concurrence C for three different values of z_{21}. We observe that the vacuum of the field can produce entanglement between the two atoms. Figures 21(a) and 21(b) show that, when the atoms are close to each other, the magnitudes of the entanglement produced in the cases $|\psi(0)\rangle = |\psi_1\rangle$ (solid red lines) and $|\psi_2\rangle$ (dashed blue lines) are significant and almost equal to each other, and almost equal to that produced by atoms in free space (see the dotted black lines). The reason is that, when the separation between the atoms is small enough, the effect of radiation modes on the entanglement is dominant with respect to that of guided modes. We observe from Fig. 21(c) that, when the separation between the atoms is large enough, the magnitudes of the entanglement produced in the cases $|\psi(0)\rangle = |\psi_1\rangle$ (solid red lines) and $|\psi_2\rangle$ (dashed blue lines) are small but not negligible, and differ significantly from each other and from the corresponding value that is produced by two atoms in free space (see the dotted black lines). We observe from Fig. 21 that, for the parameters used, the presence of the nanofiber reduces the peak value of the generated concurrence C. However, our
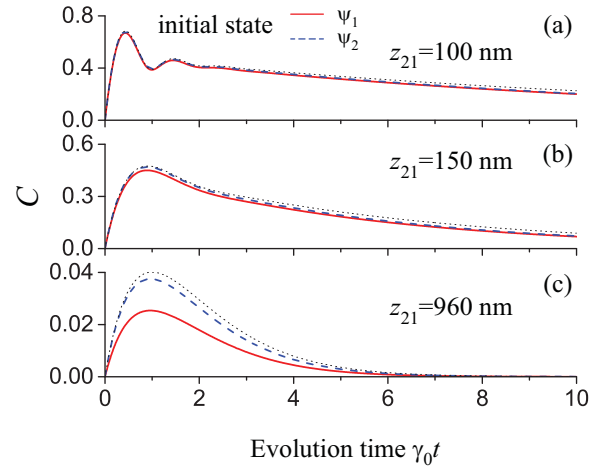

FIG. 21. Time evolution of the concurrence in the cases where the initial state of the two-atom system is $|\psi(0)\rangle = |\psi_1\rangle$ (solid red lines) or $|\psi_2\rangle$ (dashed blue lines). The coordinates of the atoms are $r_1 - a = r_2 - a = 200$ nm, $\varphi_1 = \varphi_2 = 0$, and $z_2 - z_1 = 100$ nm (a), 150 nm (b), and 960 nm (c). Other parameters are as for Figs. 2 and 4. The dotted black lines are for the case of two atoms in free space.

additional calculations that are not shown here indicate that, depending on the parameters, the presence of the nanofiber may reduce or increase the peak value of C (see also Fig. 22).

When the separation between the atoms is much larger than the wavelength of light, the effect of radiation modes on entanglement becomes negligible while the effect of guided modes survives. In order to illustrate the ability of the vacuum guided light field to produce entanglement between two atoms with a large separation, we plot in Fig. 22 the time dependence of the concurrence produced in the case where $z_{21} = 100 \, \mu$m. We observe from the figure that, even though z_{21} is very large as compared to the wavelength of light, the vacuum guided field can produce a finite entanglement. The peak value of the produced concurrence (see the solid red and dashed blue lines) is substantially larger than the corresponding concurrence produced by the vacuum free-space field (see the dotted black line). Comparison between the solid red and
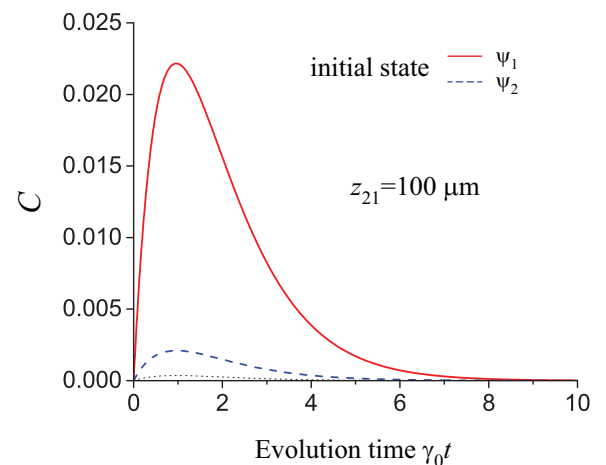

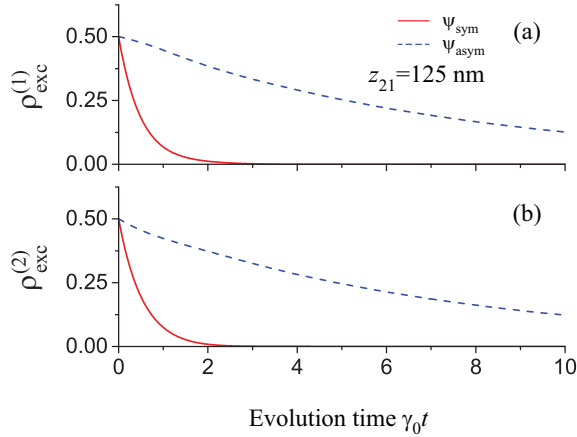FIG. 22. Same as Fig. 21 except for $z_2 - z_1 = 100 \, \mu$m.

FIG. 23. Time evolution of the populations (a) $\rho_{exc}^{(1)}$ and (b) $\rho_{exc}^{(2)}$ of the upper levels of atoms 1 and 2, respectively, in the cases where the initial state of the two-atom system is $|\psi(0)\rangle = |\psi_{sym}\rangle$ (solid red lines) or $|\psi_{asym}\rangle$ (dashed blue lines). The coordinates of the atoms are $r_1 - a = r_2 - a = 200$ nm, $\varphi_1 = \varphi_2 = 0$, and $z_2 - z_1 = 125$ nm. The dipole matrix elements of the atoms are $\mathbf{d}_1 = \mathbf{d}_2 = (d/\sqrt{2})(i, 0, -1)$, corresponding to the σ_+-polarized transitions with respect to the y quantization axis. Other parameters are as for Figs. 2 and 4.

dashed blue lines shows that the magnitude of the produced entanglement depends on the excitation transfer direction specified by the ordering of the excited and unexcited atoms in the initial atomic states $|\psi_1\rangle$ and $|\psi_2\rangle$. We emphasize that chirality is not required to generate entanglement between the atoms. Indeed, according to the dotted curves in Fig. 21, entanglement between the atoms can be generated even when the atoms are in free space. This entanglement decreases quickly with increasing separation between the atoms. Due to the cooperation between the atoms through the guided modes, a substantial entanglement can be generated even when the atoms are far away from each other. Due to the chirality of the interaction, the produced entanglement depends on the excitation transfer direction (see Fig. 22). Our results are consistent with the results of Ref. [45] for spontaneous generation of entanglement between two qubits chirally coupled to a one-dimensional waveguide.

2. Symmetric and antisymmetric superposition states

We now consider the cases where the initial state of the two-atom system is $|\psi(0)\rangle = |\psi_{sym}\rangle$ or $|\psi_{asym}\rangle$. Here, $|\psi_{sym}\rangle = (|+-\rangle + e^{-i\varphi_{12}}|-+\rangle)/\sqrt{2}$ and $|\psi_{asym}\rangle = (|+-\rangle - e^{-i\varphi_{12}}|-+\rangle)/\sqrt{2}$ are the symmetric and antisymmetric superposition states, with φ_{12} being the phase of the cross-atom decay coefficient γ_{12}.

We plot in Fig. 23 the excited-state populations $\rho_{exc}^{(1)}$ and $\rho_{exc}^{(2)}$ of atoms 1 and 2, respectively, calculated for the cases where the initial state of the two-atom system is $|\psi(0)\rangle = |\psi_{sym}\rangle$ (solid red lines) or $|\psi_{asym}\rangle$ (dashed blue lines). The two atoms are aligned along the fiber axis with the separation $z_{21} = z_2 - z_1 = 125$ nm. We observe from the figure that the decay of the excited-level populations of the atoms in the case of the initial state $|\psi_{sym}\rangle$ (solid red lines) is much faster than that in the case of the initial state $|\psi_{asym}\rangle$ (dashed blue lines).
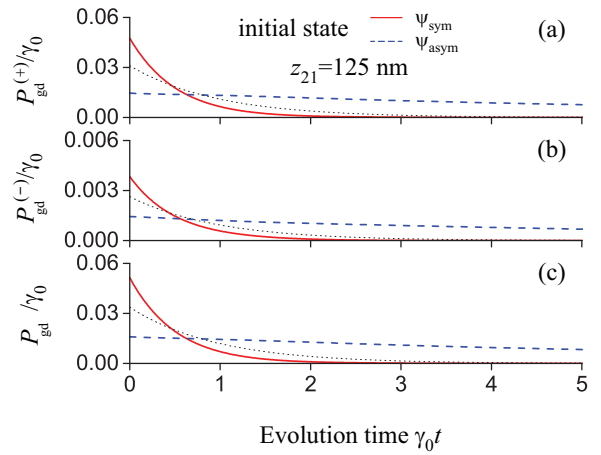

FIG. 24. Time evolution of the photon fluxes (a) $P_{gd}^{(+)}$, (b) $P_{gd}^{(-)}$, and (c) P_{gd} in the cases where the initial state of the two-atom system is $|\psi(0)\rangle = |\psi_{sym}\rangle$ (solid red lines) or $|\psi_{asym}\rangle$ (dashed blue lines). Other parameters are as for Figs. 2, 4, and 23. The fluxes are normalized to the decay rate γ_0 of a single atom in free space. The dotted black lines are for the case of a single excited atom.

Comparison between Figs. 23(a) and 23(b) shows that the decay of $\rho_{exc}^{(1)}$ is almost the same as the decay of $\rho_{exc}^{(2)}$ in the both cases.

We plot in Fig. 24 the time evolution of the fluxes $P_{gd}^{(+)}$ and $P_{gd}^{(-)}$ of photons emitted into guided modes in the positive and negative directions of the fiber axis, respectively, and the total guided-photon flux P_{gd}, calculated for the cases where the initial state of the two-atom system is $|\psi(0)\rangle = |\psi_{sym}\rangle$ (solid red lines) or $|\psi_{asym}\rangle$ (dashed blue lines). We observe that the photon flux $P_{gd}^{(+)}$ for the positive direction [see Fig. 24(a)] is about one order larger than the photon flux $P_{gd}^{(-)}$ for the negative direction [see Fig. 24(b)]. We also observe that the photon fluxes for the initial states $|\psi_{sym}\rangle$ (solid red lines) and $|\psi_{asym}\rangle$ (dashed blue lines) are different from each other. At the onset of the evolution, the photon fluxes in the cases of $|\psi_{sym}\rangle$ (see solid red lines) and $|\psi_{asym}\rangle$ (see dashed blue lines) are, respectively, larger and smaller than the photon fluxes in the case of a single excited atom (see the dotted black lines). When the time is large enough, the opposite relationships hold true. Thus, the states $|\psi_{sym}\rangle$ and $|\psi_{asym}\rangle$ correspond to superradiant and subradiant states [52,57,58] for guided modes in the case considered.

We plot in Fig. 25 the time evolution of the flux P_{rad} of photons emitted into radiation modes and the total photon flux P_{tot} for the parameters of Fig. 24. We observe that the fluxes P_{rad} and P_{tot} in the case of $|\psi(0)\rangle = |\psi_{sym}\rangle$ (solid red lines) are different from those in the case of $|\psi_{asym}\rangle$ (dashed blue lines). When the interaction time is short enough, the values of P_{rad} and P_{tot} in the case of $|\psi(0)\rangle = |\psi_{sym}\rangle$ (solid red lines) are larger than the corresponding values in the case of a single excited atom (dotted black lines). Meanwhile, when the interaction time is not too long, the values of P_{rad} and P_{tot} in the case of $|\psi(0)\rangle = |\psi_{asym}\rangle$ (dashed blue lines) are smaller than the corresponding values in the case of a single excited atom (dotted black lines). Thus, the superposition states $|\psi_{sym}\rangle$ and

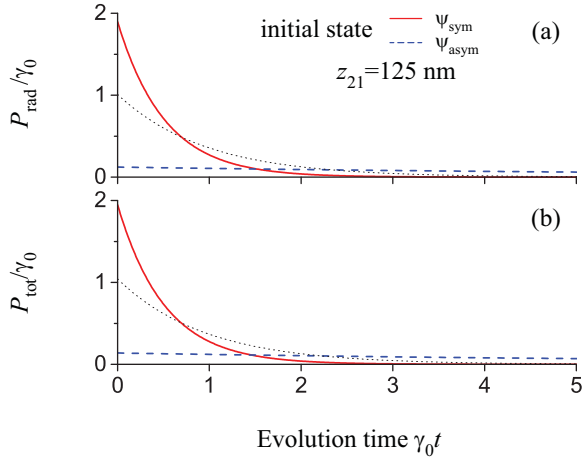FIG. 25. Time evolution of the photon fluxes (a) P_{rad} and (b) P_{tot} in the cases where the initial state of the two-atom system is $|\psi(0)\rangle = |\psi_{\mathrm{sym}}\rangle$ (solid red lines) or $|\psi_{\mathrm{asym}}\rangle$ (dashed blue lines). Other parameters are as for Figs. 2, 4, and 23. The fluxes are normalized to the decay rate γ_0 of a single atom in free space. The dotted black lines are for the case of a single excited atom.

$|\psi_{\mathrm{asym}}\rangle$ are also superradiant and subradiant states [52,57,58] for radiation modes in the case considered.

It is interesting to note that an atomic superposition state can be a superradiant state for radiation modes but a subradiant state for guided modes. In order to illustrate such a situation, we plot in Figs. 26–28 the results of calculations for the case where $z_{21} = 300$ nm. Figure 26 shows that the decay of the excited-level populations in the case of $|\psi_{\mathrm{sym}}\rangle$ (solid red lines) is faster than that in the case of $|\psi_{\mathrm{asym}}\rangle$ (dashed blue lines). Meanwhile, according to Fig. 27, the fluxes of photon emitted into radiation modes in the cases of the initial states $|\psi_{\mathrm{sym}}\rangle$ (solid red lines) and $|\psi_{\mathrm{asym}}\rangle$ (dashed blue lines) are, respectively, weaker and stronger than those in the case of a single excited atom (dotted black lines). Thus, the superposition states $|\psi_{\mathrm{sym}}\rangle$ and $|\psi_{\mathrm{asym}}\rangle$ are, respectively, subradiant and superradiant states for emission into guided modes. The result of Figs. 26 and 27 do no contradict the
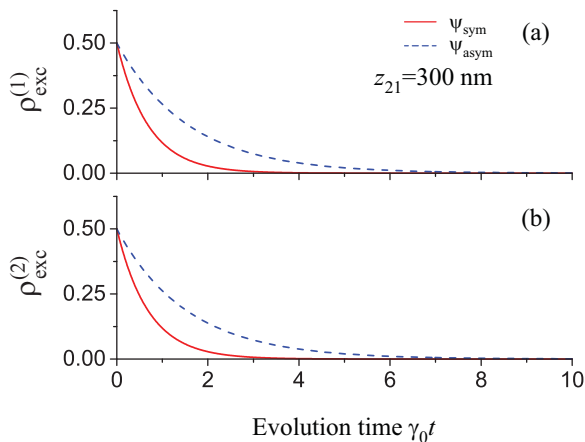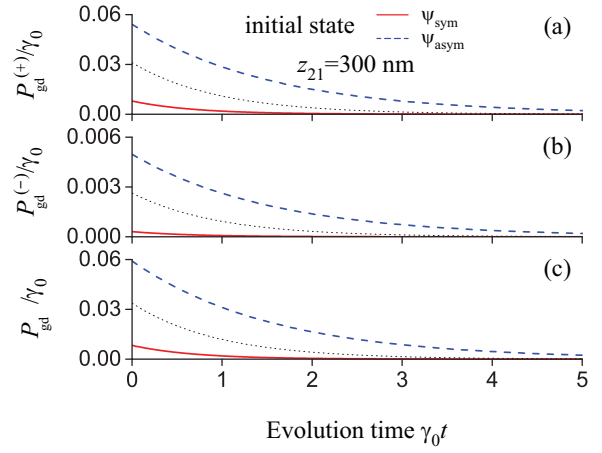
FIG. 27. Same as Fig. 24 but for $z_{21} = 300$ nm.

energy conservation law. Indeed, as already mentioned above, in addition to emission into guided modes, there is emission into radiation modes. According to Fig. 28, the fluxes of photon emitted into guided modes in the cases of the initial states $|\psi_{\mathrm{sym}}\rangle$ (solid red lines) and $|\psi_{\mathrm{asym}}\rangle$ (dashed blue lines) are, respectively, stronger and weaker than those in the case of a single excited atom (dotted black lines). This result means that the superposition states $|\psi_{\mathrm{sym}}\rangle$ and $|\psi_{\mathrm{asym}}\rangle$ are, respectively, superradiant and subradiant states for emission into radiation modes as well as for the total emission into both types of modes. These collective effects are opposite to those collective effects occurring in emission into guided modes. The difference is caused by the action of cross-atom interference on the emission rate.

We plot in Figs. 29 and 30 the dependencies of the mean emitted guided photon numbers on the axial atomic separation z_{21} and the atom-to-surface distance $r - a$, respectively. We observe from Figs. 29 and 30 that the mean photon number $N_{\mathrm{gd}}^{(+)}$ for the positive direction is about one order larger than the mean photon number $N_{\mathrm{gd}}^{(-)}$ for the negative direction. It is clear from the figures that the mean emitted guided photon number
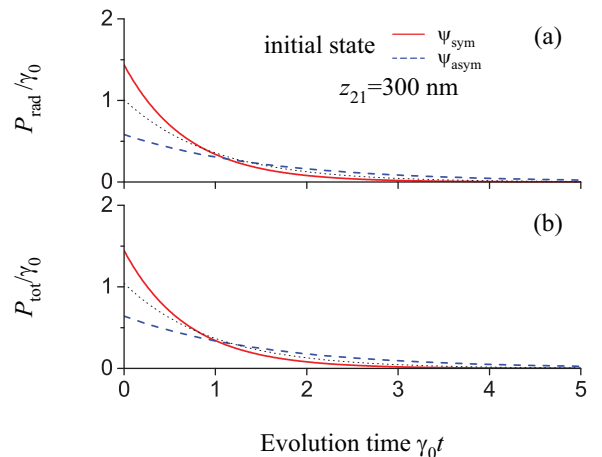

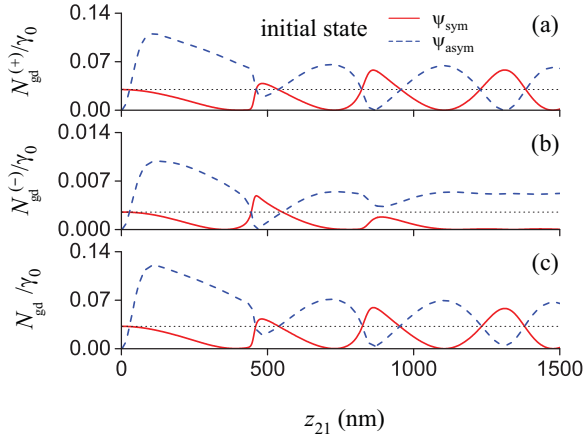FIG. 26. Same as Fig. 23 but for $z_{21} = 300$ nm.

FIG. 28. Same as Fig. 25 but for $z_{21} = 300$ nm.

FIG. 29. Dependencies of the mean emitted photon numbers (a) $N_{\mathrm{gd}}^{(+)}$, (b) $N_{\mathrm{gd}}^{(-)}$, and (c) N_{gd} on the axial separation z_{21} between the atoms in the cases where the initial state of the two-atom system is $|\psi(0)\rangle = |\psi_{\mathrm{sym}}\rangle$ (solid red lines) or $|\psi_{\mathrm{asym}}\rangle$ (dashed blue lines). The radial and azimuthal coordinates of the atoms are $r_1 - a = r_2 - a = 200\,\mathrm{nm}$ and $\varphi_1 = \varphi_2 = 0$, respectively. Other parameters are as for Figs. 2, 4, and 23. The dotted black lines are for the case of a single excited atom.

N_{gd} and its directional components $N_{\mathrm{gd}}^{(+)}$ and $N_{\mathrm{gd}}^{(-)}$ depend on the axial atomic separation z_{21}, the atom-surface distance $r - a$, and the initial superposition state. When we compare the solid red and dashed blue lines of Fig. 29 with the dotted lines of this figure, we see that, depending on the axial atomic separation z_{21} and the initial superposition state, the probability of emitting a photon into guided modes may be enhanced or suppressed. We observe from Fig. 29 that, depending on z_{21}, the values of $N_{\mathrm{gd}}^{(+)}$, $N_{\mathrm{gd}}^{(-)}$, and N_{gd} in the case of the initial state $|\psi(0)\rangle = |\psi_{\mathrm{sym}}\rangle$ (solid red lines) may be larger or smaller than the corresponding values in the case of the initial state $|\psi(0)\rangle = |\psi_{\mathrm{asym}}\rangle$ (dashed blue lines). We observe from Fig. 29
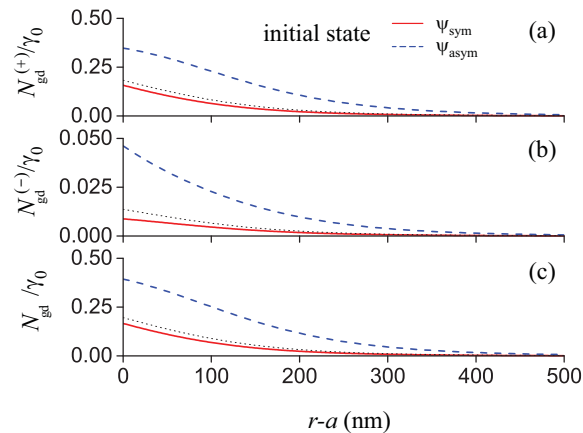

FIG. 30. Dependencies of the mean emitted photon numbers (a) $N_{\mathrm{gd}}^{(+)}$, (b) $N_{\mathrm{gd}}^{(-)}$, and (c) N_{gd} on the distance $r - a$ from the atoms to the fiber surface in the cases where the initial state of the two-atom system is $|\psi(0)\rangle = |\psi_{\mathrm{sym}}\rangle$ (solid red lines) or $|\psi_{\mathrm{asym}}\rangle$ (dashed blue lines). The coordinates of the atoms are $r_1 = r_2 = r$, $\varphi_1 = \varphi_2 = 0$, and $z_2 - z_1 = 150\,\mathrm{nm}$. Other parameters are as for Figs. 2, 4, and 23. The dotted lines are for the case of a single excited atom.

that there exist regions of z_{21} where N_{gd} and its directional components $N_{\mathrm{gd}}^{(+)}$ and $N_{\mathrm{gd}}^{(-)}$ for the two-atom case (see the solid red and dashed blue lines) are several times larger than the corresponding values for a single excited atom (see the dotted black lines). Also, there exist regions of z_{21} where N_{gd} and its directional components $N_{\mathrm{gd}}^{(+)}$ and $N_{\mathrm{gd}}^{(-)}$ for the two-atom case are almost zero. These features are signatures of the collective effect in spontaneous emission into guided modes. We emphasize again that, since the total number of emitted photons is fixed as given by the total initial excitation of the atoms, an increase or a decrease in the mean number of photons emitted into guided modes is associated with a decrease or an increase, respectively, in the mean number of photons emitted into radiation modes.

V. SUMMARY

In this paper, we have studied the coupling between two two-level atoms with arbitrarily polarized dipoles in the vicinity of a nanofiber. We have derived the master equation for the atoms interacting with the vacuum of the field in the guided and radiation modes of the nanofiber. We have obtained the expressions for the single-atom and cross-atom decay coefficients and their directional components. We have also got the expressions for the dipole-dipole interaction coefficients. We have studied numerically the case where the atomic dipoles are circularly polarized and, consequently, the rate of emission depends on the propagation direction and the radiative interaction between the atoms is chiral. We have examined the time evolution of the atoms for different initial one-excitation states. We have calculated the fluxes and mean numbers of photons spontaneously emitted into guided modes in the positive and negative directions of the fiber axis. We have shown that the chiral radiative coupling modifies the collective emission of the atoms. We have observed that the modifications strongly depend on the initial state of the atomic system, the radiative transfer direction, the distance between the atoms, and the distance from the atoms to the fiber surface.

APPENDIX A: GUIDED MODES OF A NANOFIBER

Consider a nanofiber that is a silica cylinder of radius a and refractive index n_1 and is surrounded by an infinite background medium of refractive index n_2, where $n_2 < n_1$. The radius of the nanofiber is well below a given free-space wavelength λ of light. Therefore, the nanofiber supports only the hybrid fundamental modes HE_{11} corresponding to the given wavelength λ [50]. The light field in such a mode is strongly guided. It penetrates into the outside of the nanofiber in the form of an evanescent wave carrying a significant fraction of energy [59]. For a fundamental guided mode HE_{11} of a light field of frequency ω (free-space wavelength $\lambda = 2\pi c/\omega$ and free-space wave number $k = \omega/c$), the propagation

constant β is determined by the fiber eigenvalue equation [50]

$$
\frac{J_0(ha)}{ha\,J_1(ha)} = -\frac{n_1^2 + n_2^2}{2n_1^2}\frac{K_1'(qa)}{qa\,K_1(qa)} + \frac{1}{h^2a^2}
$$
$$
- \left[\left(\frac{n_1^2 - n_2^2}{2n_1^2}\frac{K_1'(qa)}{qa\,K_1(qa)} \right)^2 \right.
$$
$$
\left. + \frac{\beta^2}{n_1^2 k^2}\left(\frac{1}{q^2a^2} + \frac{1}{h^2a^2} \right)^2 \right]^{1/2}. \quad \text{(A1)}
$$

Here, the parameters $h = (n_1^2 k^2 - \beta^2)^{1/2}$ and $q = (\beta^2 - n_2^2 k^2)^{1/2}$ characterize the fields inside and outside the fiber, respectively. The notations J_n and K_n stand for the Bessel functions of the first kind and the modified Bessel functions of the second kind, respectively.

According to Ref. [50], the cylindrical-coordinate vector components of the profile function $\mathbf{e}(\mathbf{r})$ of the electric part of the fundamental guided mode that propagates in the forward ($+\hat{\mathbf{z}}$) direction and is counterclockwise quasicircularly polarized are given, for $r < a$, by

$$
e_r = iC\frac{q}{h}\frac{K_1(qa)}{J_1(ha)}[(1-s)J_0(hr) - (1+s)J_2(hr)],
$$
$$
e_\varphi = -C\frac{q}{h}\frac{K_1(qa)}{J_1(ha)}[(1-s)J_0(hr) + (1+s)J_2(hr)],
$$
$$
e_z = C\frac{2q}{\beta}\frac{K_1(qa)}{J_1(ha)}J_1(hr), \quad \text{(A2)}
$$

and, for $r > a$, by

$$
e_r = iC[(1-s)K_0(qr) + (1+s)K_2(qr)],
$$
$$
e_\varphi = -C[(1-s)K_0(qr) - (1+s)K_2(qr)],
$$
$$
e_z = C\frac{2q}{\beta}K_1(qr). \quad \text{(A3)}
$$

Here, the parameter s is defined as

$$
s = \frac{1/h^2a^2 + 1/q^2a^2}{J_1'(ha)/ha\,J_1(ha) + K_1'(qa)/qa\,K_1(qa)}. \quad \text{(A4)}
$$

The parameter C is the normalization coefficient. We take C to be a positive real number and use the normalization condition

$$
\int_0^{2\pi} d\varphi \int_0^\infty n_{\text{ref}}^2 |\mathbf{e}|^2 r\,dr = 1. \quad \text{(A5)}
$$

Here, $n_{\text{ref}}(r) = n_1$ for $r < a$, and $n_{\text{ref}}(r) = n_2$ for $r > a$. We note that the axial component e_z is significant in the case of nanofibers [59]. This makes guided modes of nanofibers very different from plane-wave modes of the field in free space and from guided modes of conventional (weakly guiding) fibers [50,59].

We label quasicircularly polarized fundamental guided modes HE_{11} by using a mode index $\mu = (\omega, f, l)$, where ω is the mode frequency, $f = +1$ or -1 (or simply $+$ or $-$) denotes the forward ($+\hat{\mathbf{z}}$) or backward ($-\hat{\mathbf{z}}$) propagation direction, respectively, and $l = +1$ or -1 (or simply $+$ or $-$) denotes the counterclockwise or clockwise circulation, respectively, of the transverse component of the polarization around the axis $+\hat{\mathbf{z}}$. In the cylindrical coordinates, the components of the

profile function $\mathbf{e}^{(\mu)}(\mathbf{r})$ of the electric part of the quasicircularly polarized fundamental guided mode μ are given by

$$
e_r^{(\mu)} = e_r,
$$
$$
e_\varphi^{(\mu)} = le_\varphi, \quad \text{(A6)}
$$
$$
e_z^{(\mu)} = fe_z.
$$

Consequently, the profile function of the quasicircularly polarized mode (ω, f, l) can be written as

$$
\mathbf{e}^{(\omega f l)} = \hat{\mathbf{r}}e_r^{(\omega f l)} + \hat{\boldsymbol{\varphi}}e_\varphi^{(\omega f l)} + \hat{\mathbf{z}}e_z^{(\omega f l)}
$$
$$
= \hat{\mathbf{r}}e_r + l\hat{\boldsymbol{\varphi}}e_\varphi + f\hat{\mathbf{z}}e_z, \quad \text{(A7)}
$$

where the notations $\hat{\mathbf{r}} = \hat{\mathbf{x}}\cos\varphi + \hat{\mathbf{y}}\sin\varphi$, $\hat{\boldsymbol{\varphi}} = -\hat{\mathbf{x}}\sin\varphi + \hat{\mathbf{y}}\cos\varphi$, and $\hat{\mathbf{z}}$ stand for the unit basis vectors of the cylindrical coordinate system $\{r, \varphi, z\}$. Here, $\hat{\mathbf{x}}$ and $\hat{\mathbf{y}}$ are the unit basis vectors of the Cartesian coordinate system for the fiber transverse plane xy.

We have the following symmetry relations:

$$
e_r^{(\omega, f, l)} = e_r^{(\omega, -f, l)} = e_r^{(\omega, f, -l)},
$$
$$
e_\varphi^{(\omega, f, l)} = e_\varphi^{(\omega, -f, l)} = -e_\varphi^{(\omega, f, -l)}, \quad \text{(A8)}
$$
$$
e_z^{(\omega, f, l)} = -e_z^{(\omega, -f, l)} = e_z^{(\omega, f, -l)},
$$

and

$$
e_r^{(\mu)*} = -e_r^{(\mu)}, \quad e_\varphi^{(\mu)*} = e_\varphi^{(\mu)}, \quad e_z^{(\mu)*} = e_z^{(\mu)}. \quad \text{(A9)}
$$

APPENDIX B: RADIATION MODES OF A NANOFIBER

For the radiation modes, we have $-kn_2 < \beta < kn_2$. The characteristic parameters for the field in the inside and outside of the fiber are $h = \sqrt{k^2 n_1^2 - \beta^2}$ and $q = \sqrt{k^2 n_2^2 - \beta^2}$, respectively. The mode functions of the electric parts of the radiation modes $\nu = (\omega\beta ml)$ [50] are given, for $r < a$, by

$$
e_r^{(\nu)} = \frac{i}{h^2}\left[\beta h A J_m'(hr) + im\frac{\omega\mu_0}{r}B J_m(hr) \right],
$$
$$
e_\varphi^{(\nu)} = \frac{i}{h^2}\left[im\frac{\beta}{r}A J_m(hr) - h\omega\mu_0 B J_m'(hr) \right], \quad \text{(B1)}
$$
$$
e_z^{(\nu)} = A J_m(hr),
$$

and, for $r > a$, by

$$
e_r^{(\nu)} = \frac{i}{q^2}\sum_{j=1,2}\left[\beta q C_j H_m^{(j)\prime}(qr) + im\frac{\omega\mu_0}{r}D_j H_m^{(j)}(qr) \right],
$$
$$
e_\varphi^{(\nu)} = \frac{i}{q^2}\sum_{j=1,2}\left[im\frac{\beta}{r}C_j H_m^{(j)}(qr) - q\omega\mu_0 D_j H_m^{(j)\prime}(qr) \right],
$$
$$
e_z^{(\nu)} = \sum_{j=1,2} C_j H_m^{(j)}(qr). \quad \text{(B2)}
$$

Here, A and B as well as C_j and D_j with $j = 1,2$ are coefficients. The coefficients C_j and D_j are related to the coefficients A and B as [60]

$$
C_j = (-1)^j\frac{i\pi q^2 a}{4n_2^2}(AL_j + i\mu_0 cBV_j),
$$
$$
D_j = (-1)^{j-1}\frac{i\pi q^2 a}{4}(i\epsilon_0 cAV_j - BM_j), \quad \text{(B3)}
$$

where

$$V_j = \frac{mk\beta}{ah^2q^2}\left(n_2^2 - n_1^2\right)J_m(ha)H_m^{(j)*}(qa),$$

$$M_j = \frac{1}{h}J_m'(ha)H_m^{(j)*}(qa) - \frac{1}{q}J_m(ha)H_m^{(j)*\prime}(qa), \quad \text{(B4)}$$

$$L_j = \frac{n_1^2}{h}J_m'(ha)H_m^{(j)*}(qa) - \frac{n_2^2}{q}J_m(ha)H_m^{(j)*\prime}(qa).$$

We specify two polarizations by choosing $B = i\eta A$ and $B = -i\eta A$ for $l = +$ and $l = -$, respectively. We take A to be a real number. The orthogonality of the modes requires

$$\int_0^{2\pi} d\varphi \int_0^\infty n_{\text{ref}}^2 [\mathbf{e}^{(\nu)}\mathbf{e}^{(\nu')*}]_{\beta=\beta',m=m'} \, r \, dr = N_\nu \delta_{ll'}\delta(\omega - \omega').$$

(B5)

This leads to

$$\eta = \epsilon_0 c \sqrt{\frac{n_2^2|V_j|^2 + |L_j|^2}{|V_j|^2 + n_2^2|M_j|^2}}. \quad \text{(B6)}$$

The constant N_ν is given by

$$N_\nu = \frac{8\pi\omega}{q^2}\left(n_2^2|C_j|^2 + \frac{\mu_0}{\epsilon_0}|D_j|^2\right). \quad \text{(B7)}$$

We use the normalization $N_\nu = 1$.

We have the following symmetry relations:

$$e_r^{(\omega,\beta,m,l)} = -e_r^{(\omega,-\beta,m,-l)},$$

$$e_\varphi^{(\omega,\beta,m,l)} = -e_\varphi^{(\omega,-\beta,m,-l)}, \quad \text{(B8)}$$

$$e_z^{(\omega,\beta,m,l)} = e_z^{(\omega,-\beta,m,-l)},$$

$$e_r^{(\omega,\beta,m,l)} = (-1)^m e_r^{(\omega,\beta,-m,-l)},$$

$$e_\varphi^{(\omega,\beta,m,l)} = (-1)^{m+1}e_\varphi^{(\omega,\beta,-m,-l)}, \quad \text{(B9)}$$

$$e_z^{(\omega,\beta,m,l)} = (-1)^m e_z^{(\omega,\beta,-m,-l)},$$

and

$$e_r^{(\nu)*} = -e_r^{(\nu)}, \quad e_\varphi^{(\nu)*} = e_\varphi^{(\nu)}, \quad e_z^{(\nu)*} = e_z^{(\nu)}. \quad \text{(B10)}$$

---

[1] J. I. Gersten and A. Nitzan, Chem. Phys. Lett. **104**, 31 (1984).

[2] L. M. Folan, S. Arnold, and S. D. Druger, Chem. Phys. Lett. **118**, 322 (1985).

[3] S. Arnold, S. Holler, and S. D. Druger, *Optical Processes in Microcavities* (World Scientific, Singapore, 1996), pp. 285–313.

[4] G. S. Agarwal and S. Dutta Gupta, Phys. Rev. A **57**, 667 (1998).

[5] M. Hopmeier, W. Guss, M. Deussen, E. O. Göbel, and R. F. Mahrt, Phys. Rev. Lett. **82**, 4118 (1999).

[6] W. L. Barnes and P. Andrews, Nature (London) **400**, 505 (1999); P. Andrews and W. L. Barnes, Science **290**, 785 (2000).

[7] R. L. Hartman and P. T. Leung, Phys. Rev. B **64**, 193308 (2001).

[8] D. M. Basko, J. Lumin. **110**, 359 (2004); D. M. Basko, F. Bassani, G. C. La Rocca, and V. M. Agranovich, Phys. Rev. B **62**, 15962 (2000).

[9] H. T. Dung, L. Knöll, and D.-G. Welsch, Phys. Rev. A **66**, 063810 (2002).

[10] S. Götzinger, L. de S. Menezes, A. Mazzei, S. Kühn, V. Sandoghdar, and O. Benson, Nano Lett. **6**, 1151 (2006).

[11] F. Schleifenbaum, A. M. Kern, A. Konrad, and A. J. Meixner, Phys. Chem. Chem. Phys. **16**, 12812 (2014).

[12] R. Chang, P. T. Leung, and D. P. Tsai, Opt. Express **22**, 27451 (2014).

[13] S. A. Crooker, J. A. Hollingsworth, S. Tretiak, and V. I. Klimov, Phys. Rev. Lett. **89**, 186802 (2002).

[14] D. Kozawa, A. Carvalho, I. Verzhbitskiy, F. Giustiniano, Y. Miyauchi, S. Mouri, A. H. Castro Neto, K. Matsuda, and G. Eda, Nano Lett. **16**, 4087 (2016).

[15] P. Andrew and W. L. Barnes, Science **306**, 1002 (2004).

[16] D. Bouchet, D. Cao, R. Carminati, Y. De Wilde, and V. Krachmalnicoff, Phys. Rev. Lett. **116**, 037401 (2016).

[17] C. Hettich, C. Schmitt, J. Zitzmann, S. Kühn, I. Gerhardt, and V. Sandoghdar, Science **298**, 385 (2002).

[18] Y. Zhang *et al.*, Nature (London) **531**, 623 (2016).

[19] O. Keller, *Quantum Theory of Near-Field Electrodynamics* (Springer-Verlag, Berlin, 2011).

[20] L. Novotny and B. Hecht, *Principles of Nano-Optics* (Cambridge University Press, Cambridge, 2012).

[21] V. V. Klimov and V. S. Letokhov, Phys. Rev. A **58**, 3235 (1998).

[22] H. T. Dung, S. Scheel, D.-G. Welsch, and L. Knöll, J. Opt. B **4**, S169 (2002).

[23] H. Nha and W. Jhe, Phys. Rev. A **56**, 2213 (1997).

[24] V. V. Klimov and M. Ducloy, Phys. Rev. A **69**, 013812 (2004).

[25] Fam Le Kien, S. D. Gupta, V. I. Balykin, and K. Hakuta, Phys. Rev. A **72**, 032509 (2005).

[26] Fam Le Kien, S. D. Gupta, K. P. Nayak, and K. Hakuta, Phys. Rev. A **72**, 063815 (2005).

[27] Fam Le Kien and A. Rauschenbeutel, Phys. Rev. A **90**, 023805 (2014).

[28] J. Petersen, J. Volz, and A. Rauschenbeutel, Science **346**, 67 (2014).

[29] R. Mitsch, C. Sayrin, B. Albrecht, P. Schneeweiss, and A. Rauschenbeutel, Nat. Commun. **5**, 5713 (2014).

[30] Fam Le Kien and A. Rauschenbeutel, Phys. Rev. A **90**, 063816 (2014).

[31] S. Scheel, S. Y. Buhmann, C. Clausen, and P. Schneeweiss, Phys. Rev. A **92**, 043819 (2015).

[32] C. Sayrin, C. Junge, R. Mitsch, B. Albrecht, D. O'Shea, P. Schneeweiss, J. Volz, and A. Rauschenbeutel, Phys. Rev. X **5**, 041036 (2015).

[33] A. V. Dooghin, N. D. Kundikova, V. S. Liberman, and B. Y. Zeldovich, Phys. Rev. A **45**, 8204 (1992); V. S. Liberman and B. Y. Zeldovich, *ibid.* **46**, 5199 (1992); M. Y. Darsht, B. Y. Zeldovich, I. V. Kataevskaya, and N. D. Kundikova, JETP **80**, 817 (1995) [Zh. Eksp. Teor. Phys. **107**, 1464 (1995)].

[34] For a review, see K. Y. Bliokh, A. Aiello, and M. A. Alonso, in *The Angular Momentum of Light*, edited by D. L. Andrews and M. Babiker (Cambridge University Press, Cambridge, 2012), p. 174.

[35] For a more recent review, see K. Y. Bliokh, F. J. Rodriguez-Fortuño, F. Nori, and A. V. Zayats, Nat. Photon. **9**, 796 (2015).

[36] K. Y. Bliokh, D. Smirnova, and F. Nori, Science **348**, 1448 (2015).

[37] K. Y. Bliokh, A. Y. Bekshaev, and F. Nori, Nat. Commun. **5**, 3300 (2014).

[38] For a review, see A. Aiello, P. Banzer, M. Neugebauer, and G. Leuchs, Nat. Photon. **9**, 789 (2015).

[39] P. Lodahl, S. Mahmoodian, S. Stobbe, P. Schneeweiss, J. Volz, A. Rauschenbeutel, H. Pichler, and P. Zoller, Nature (London) **541**, 473 (2017).

[40] K. Stannigel, P. Rabl, and P. Zoller, New J. Phys. **14**, 063014 (2012).

[41] T. Ramos, H. Pichler, A. J. Daley, and P. Zoller, Phys. Rev. Lett. **113**, 237203 (2014).

[42] H. Pichler, T. Ramos, A. J. Daley, and P. Zoller, Phys. Rev. A **91**, 042116 (2015).

[43] T. Ramos, B. Vermersch, P. Hauke, H. Pichler, and P. Zoller, Phys. Rev. A **93**, 062104 (2016).

[44] B. Vermersch, T. Ramos, P. Hauke, and P. Zoller, Phys. Rev. A **93**, 063830 (2016).

[45] C. Gonzalez-Ballestero, A. Gonzalez-Tudela, F. J. Garcia-Vidal, and E. Moreno, Phys. Rev. B **92**, 155304 (2015).

[46] Z. Eldredge, P. Solano, D. Chang, and A. V. Gorshkov, Phys. Rev. A **94**, 053855 (2016).

[47] Fam Le Kien and A. Rauschenbeutel, Phys. Rev. A **93**, 043828 (2016).

[48] Q.-Z. Yuan, C.-H. Yuan, and W. Zhang, Phys. Rev. A **93**, 032517 (2016).

[49] C. M. Caves and D. D. Crouch, J. Opt. Soc. Am. B **4**, 1535 (1987); K. J. Blow, R. Loudon, S. J. D. Phoenix, and T. J. Shepherd, Phys. Rev. A **42**, 4102 (1990); P. Domokos, P. Horak, and H. Ritsch, *ibid.* **65**, 033832 (2002).

[50] See, for example, D. Marcuse, *Light Transmission Optics* (Krieger, Malabar, 1989); A. W. Snyder and J. D. Love, *Optical Waveguide Theory* (Chapman and Hall, New York, 1983).

[51] A. Takada and K. Ujihara, Opt. Commun. **160**, 146 (1999).

[52] G. S. Agarwal, *Quantum Optics* (Cambridge University Press, Cambridge, 2013).

[53] R. H. Lehmberg, Phys. Rev. A **2**, 883 (1970).

[54] G. V. Varada and G. S. Agarwal, Phys. Rev. A **45**, 6721 (1992).

[55] W. K. Wootters, Phys. Rev. Lett. **80**, 2245 (1998).

[56] R. Tanaś and Z. Ficek, J. Opt. B **6**, S90 (2004).

[57] R. H. Dicke, Phys. Rev. **93**, 99 (1954).

[58] M. Gross and S. Haroche, Phys. Rep. **93**, 301 (1982).

[59] Fam Le Kien, J. Q. Liang, K. Hakuta, and V. I. Balykin, Opt. Commun. **242**, 445 (2004); L. Tong, J. Lou, and E. Mazur, Opt. Express **12**, 1025 (2004).

[60] T. Søndergaard and B. Tromborg, Phys. Rev. A **64**, 033812 (2001).